

An Infrared Photometric and Spectroscopic Study of Post-AGB Stars

V. Venkata Raman^{1*}, B.G. Anandarao^{1 †}, P. Janardhan^{1 ‡} and R. Pandey^{2 §}

¹*Physical Research Laboratory (PRL), Navrangpura, Ahmedabad - 380009, India*

²*Physics Department, M.L.S. University, Udaipur, India*

ABSTRACT

We present here *Spitzer* mid-infrared (IR) spectra and modeling of the spectral energy distribution (SED) of a selection of post-Asymptotic Giant Branch (PAGB) stars. The mid-IR spectra of majority of these sources showed spectral features such as polycyclic aromatic hydrocarbons (PAHs) and silicates in emission. Our results from SED modeling showed interesting trends of dependency between the photospheric and circumstellar parameters. A trend of dependency is also noticed between the ratios of equivalent widths (EWs) of various vibrational modes of PAHs and the photospheric temperature T_* and model-derived stellar parameters for the sample stars. The PAGB mass loss rates derived from the SED models are found to be higher than those for the AGB stars. In a few objects, low and high excitation fine structure emission lines were identified, indicating their advanced stage of evolution. Further, IR vibration modes of fullerene (C_{60}) were detected for the first time in the PAGB star IRAS 21546+4721.

Key words: Stars: AGB and post-AGB – Stars: circumstellar matter – Stars: evolution – Stars: mass-loss – ISM: dust, extinction – Infrared: stars – Techniques: spectroscopic

* vvenkat@prl.res.in

† anand@prl.res.in

‡ jerry@prl.res.in

§ pandey.rj@gmail.com

1 INTRODUCTION

Post-Asymptotic Giant Branch (PAGB) stars or proto-Planetary Nebulae (PPNe) represent the short-lived, rapidly varying and least understood phase during the evolution of intermediate mass stars towards planetary nebulae (PNe) stage ([van Winckel \(2003\)](#); [Kwok \(2007\)](#) and references therein). The evolutionary phases of PAGB and PPNe are nearly indistinguishable and here onwards we treat the two to be the same. These sources exhibit infrared excess and molecular line emission from dust and molecules in the circumstellar envelopes formed by the massloss during the AGB phase. Circumstellar dust in PAGB stars cause significant extinction in the visible region. The exact composition of the circumstellar dust grains is still a matter of debate (e.g., see [Cerrigone et al. \(2009\)](#) and [Zhang et al. \(2010\)](#)). The evolution during the PAGB phase can be identified by several spectroscopic signatures - from molecular hydrogen emission to atomic hydrogen recombination lines as well as forbidden transitions from several atoms and ions. Further, the onset of UV radiation can also be inferred from the detection of circumstellar Polycyclic Aromatic Hydrocarbons (PAHs) that are excited by absorption of soft UV radiation in carbon rich PAGB stars (e.g., [Kwok \(2004\)](#), [Tielens \(2005\)](#)). Investigation of circumstellar matter and their chemical synthesis can therefore help in probing and understanding the early stages of PN formation.

Pioneering studies had been made and reported by [Kwok et al. \(1999\)](#), [Hrivnak et al. \(2000\)](#) and the references therein on the infrared spectra of PAGB stars with particular emphasis on PAH features and other as yet unidentified features as well as on molecular hydrogen lines (e.g., [Kelly and Hrivnak \(2005\)](#) and the references therein). In the present study, we model the SEDs for a fairly large sample of PAGB stars using the available archival data covering the visible to far-infrared regions. We then endeavour to find if the model-derived circumstellar parameters indicate possible dependency on evolution of the objects.

The sample selection of the PAGB stars used in the present study is described in Section 2. In Section 3, we present mid-IR spectra of the sample sources. In Section 4 we present modeling of SEDs and in Section 5 we discuss the possible correlation between the circumstellar and photospheric parameters obtained from the SED models and also between the various PAH modes of vibration with the evolution of the central star. In Section 6 we identify a few transition objects in our sample through the detection of low and high excitation fine structure lines in the mid-IR spectra. In Section 7 we present the detection of fullerenes

in one of the sample PAGB star. In Section 8 we summarise the conclusions of the present work.

2 SAMPLE OF PAGB STARS AND PHOTOMETRIC ARCHIVAL DATA:

The sample of PAGB stars studied were selected from [Szczerba et al. \(2007\)](#). Based on their *JHK*-band magnitudes being brighter than 13-14, a total of about 71 PAGB stars were identified for the present study. From the classification scheme based on the IRAS [25-60] vs [12-25] colour-colour diagram (shown in Fig 1, see [van der Veen and Habing \(1988\)](#)), it is clear that the objects selected for the present study are much more evolved than the sources in their AGB phase considered in our earlier work ([Venkata Raman and Anandarao \(2008\)](#)). Spectral types for a number of PAGB candidates were taken from SIMBAD. For some of the objects without spectral type information from SIMBAD, we have used the spectral classification by the optical survey of [Suárez et al. \(2006\)](#). Some of the objects in the selected PAGB star samples are identified as "transition objects" by [Suárez et al. \(2006\)](#). It may be noted that there exist small (and in some cases, large) differences in spectral types of some of the common objects between SIMBAD and [Suárez et al. \(2006\)](#).

The photometric data required for constructing the SEDs in the entire visible to far-infrared region were obtained from several archives. The data on visible *UBVRI* photometry were obtained from VIZIER archives; the near-IR *JHK* bands from the 2MASS archive ([Skrutskie et al. \(2006\)](#)); mid-infrared from MSX bands at 8.3, 12.1, 14.7 and 21.3 μm ([Egan et al. \(2003\)](#)); the 3.6, 4.5, 5.8 and 8 μm bands from IRAC-*SPITZER* ([Benjamin et al. \(2003\)](#)); the mid-infrared bands at 9 and 18 μm and far-infrared bands centered around 65, 90, 140 and 160 μm were obtained from the extensive all-sky survey from *AKARI* ([Ishihara et al. \(2010\)](#)); and finally the 12, 25, 60 and 100 μm band data were obtained from *IRAS* ([Helou and Walker \(1988\)](#)) archives.

3 SPITZER SPECTRA OF PAGB OBJECTS

Spitzer public archival spectroscopic data from Infra-Red Spectrograph (IRS) on-board the *Spitzer* Space Telescope covering the mid-IR region between 5.2 and 38 μm ([Houck et al. \(2004\)](#)) were used for most of the sample stars in our present study. Most of the data used here were from the short-low (SL) and long-low (LL) modules covering 5.13 to 14.29 μm and 13.9 to 39.9 μm respectively. For a few sources, the short-high (SH -

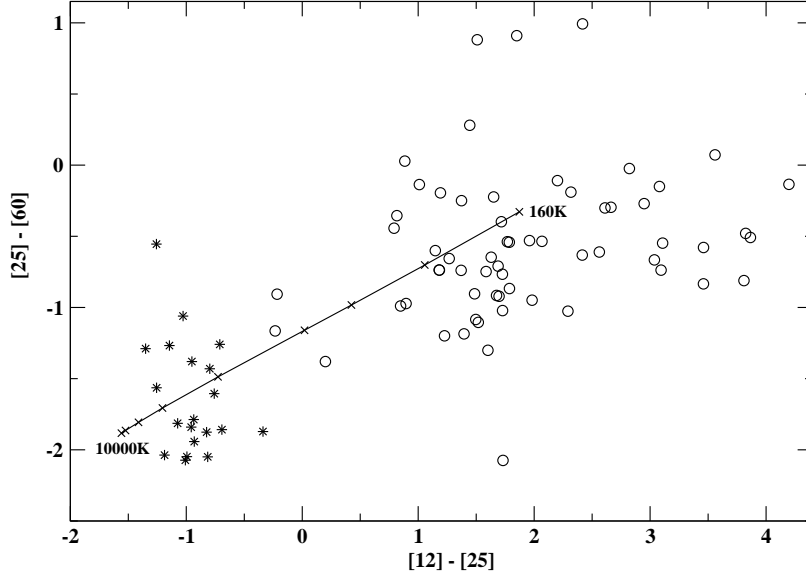


Figure 1. IRAS color-color diagram for the stars in our sample. PAGB stars (open circles) occupy positions that have very cool circumstellar shells. The AGB stars (asterisks) from Venkata Raman and Anandarao (2008) are also shown for comparison. The crosses along the line represent the black-body temperatures of 10000, 5000, 2000, 1000, 500, 300, 250, 200, 160K (see van der Veen and Habing (1988)) in the color-color space.

9.89 to 19.51 μm) and long-high (LH - 18.83 to 37.14 μm) modules were also used. The basic calibrated data (BCD) and post-BCD data from *Spitzer* archive were analysed using Spectroscopic Modeling Analysis and Reduction Tool (SMART) and *Spitzer* IRS Custom Extraction (SPICE) software packages respectively. The highly processed data products (HPDP) from the *ISO* archive (Sloan et al. (2003)) were used for a few sources in our list for which *Spitzer* data was not available.

Based on identified mid-IR spectral features, we classified our sample PAGB stars as those having (i) strong/weak or blended PAH features (ii) silicate emission, in some cases along with PAH features (iii) silicate absorption (iv) prominent broad bump around 11 μm with no PAH features and (v) nearly featureless spectra. The blended PAH refers to the blend of two or more neighboring PAH lines to form a single broad feature. Similar classification based on the presence of PAH (C-rich), silicate (O-rich) and a combination of PAH and silicate features was done by Cerrigone et al. (2009). In addition to Cerrigone et al’s classification, the present study identifies objects that have silicate absorption and those with 11 μm bump and thirdly those with featureless spectra. Table 1 provides the list of all the programme objects along with their spectral data sources and the type of dust

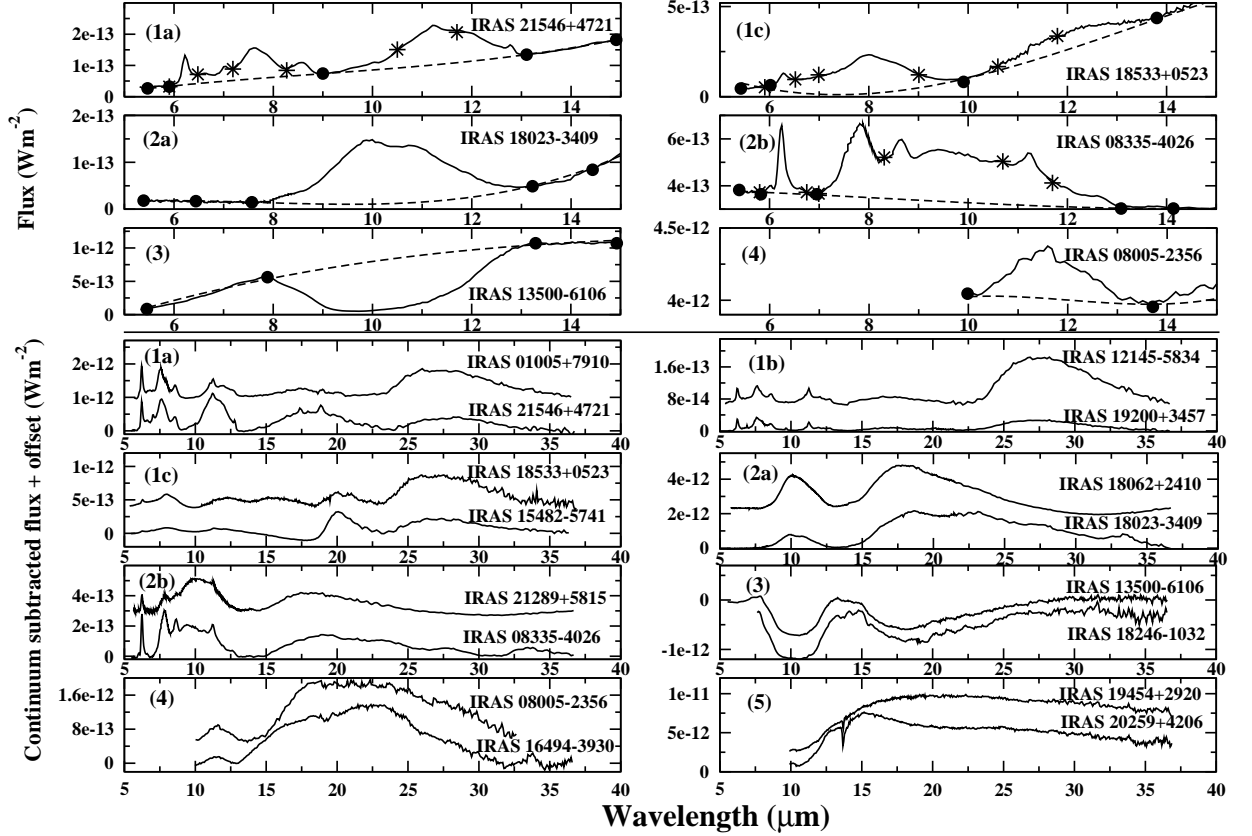


Figure 2a. Extracted raw spectra (solid curves) with pivotal points shown in filled circles and asterisks for defining the global and plateau continuum are shown in the top three (left and right) panels. Plotted in the bottom eight panels (left and right) are the continuum-subtracted *Spitzer* IRS spectra of the PAGB stars showing (1a) strong PAH features, (1b) weak PAH features (1c) blended PAH feature, (2a) silicate dust emission features, (2b) PAH + silicate emission (mixed chemistry), (3) silicate absorption (4) prominent broad bump around 11 μm and (5) featureless spectra (continuum not subtracted)

from our classification. Figure 2a gives typical spectra of the PAGB candidates depicting the above classification. The figure shows in the top three panels the raw spectra of the PAGB candidates on which pivotal points are marked (filled circle; see Spoon et al. (2007)) to define the global continuum. The continuum as defined by the pivotal points on the spectra were then fitted by a second or third order polynomial for the entire region. In the figure the continuum-subtracted spectra are shown in the bottom eight panels. The spectra for all the individual sources in each class are given in the Appendix A. Out of the 71 PAGB sources considered in the present study, 11 objects do not fall under any of the classes. In addition, 2 PAGB sources showing fine structure lines have very peculiar dust features that do not fall in the above classification. Among the remaining 58 sources, about 29% of the PAGB

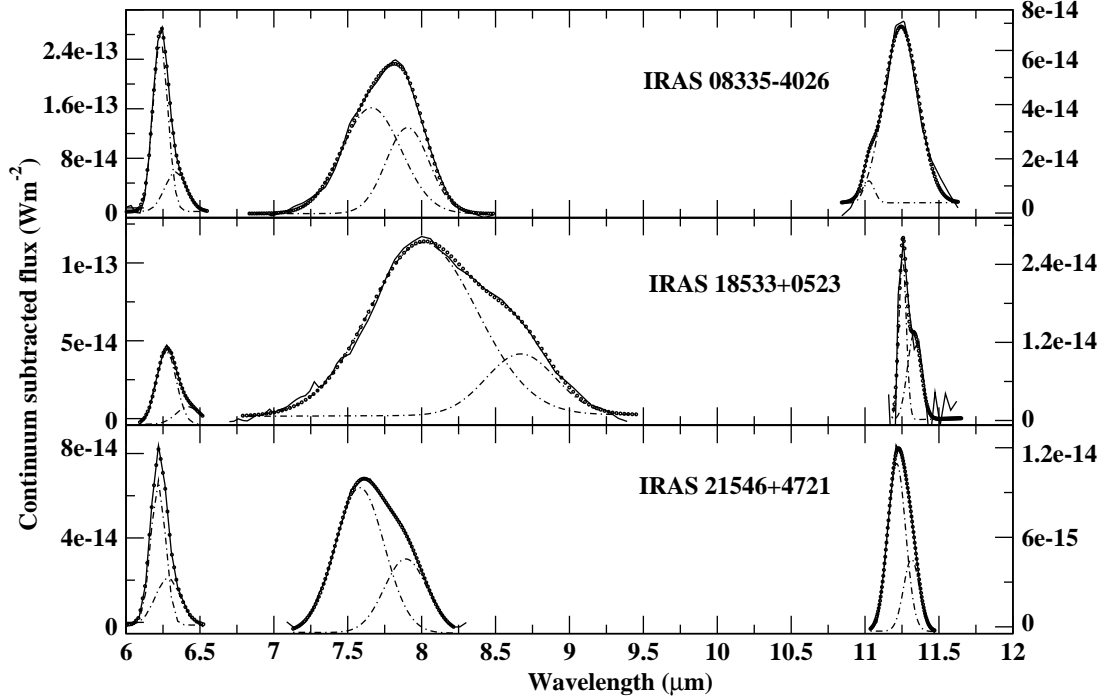


Figure 2b. Continuum-subtracted spectra of three sources chosen (from Classes 1a, 1c and 2b in Fig 2a) to illustrate multi-Gaussian decomposition of the main PAH features at 6.2, 7.7 and 11.2 μm . The fitted Gaussian profiles and their sum are represented by dot-dashed and dotted lines respectively; while the solid curves represent the continuum subtracted spectra. The flux scale on the right is for 11.2 μm feature.

sources showed strong or weak/blended PAH features, 26% showed silicate emission, 17 % of sources showed PAH along with silicate in emission (mixed chemistry), 12% of sources showed silicate absorption, 11% of sources showed 11 μm feature, 5% of sources showed featureless spectra.

Some details of the sources in different classes or categories are described below with reference to the spectra beyond 20 μm , up to 38 μm . In this spectral region the most prominent features seen are at 21 and 30 μm . Among the 17 sources that fall under the PAH category, 9 show both 21 & 30 μm features, 3 sources show only 30 μm feature and 1 source shows only 21 μm feature. The sources IRAS 04296+3429, IRAS 05113+1347, IRAS 06530-0213, IRAS 14429-4539, IRAS 15482-5741, IRAS 18533+0523, IRAS 19200+3457, IRAS 22223+4327 and IRAS 23304+6147 show both 21 & 30 μm features. The sources IRAS 01005+7910, IRAS 12145-5834 and IRAS 21546+4721 show only 30 μm feature while IRAS 07134+1005 show only 21 μm feature. All these sources show strong, blended or weak

PAH features also. The presence of 21 μm along with the observed PAH features thus depicts their carbon rich chemistry.

Silicate emissions at both 9.7 & 18 μm were observed in 15 sources. The peak position of silicate emission occurs usually at 9.7 μm , but we found that in some sources the peak occurs at longer wavelengths (≈ 10.1 to 10.2 μm). [Bouwman et al. \(2001\)](#) suggested an increase in grain size responsible for the change in the 9.7 μm peak position towards longer wavelengths. In the objects that are categorized under this section a number of sources showed features at 27 and 33 μm attributed to crystalline olivines (see [Jaeger et al. \(1998\)](#)). These sources do not show the 21 and 30 μm features. Silicate emission along with PAH (mixed chemistry) has been observed in 10 sources. A number of sources in this category also showed the presence of crystalline olivines at 27 and 33 μm . [Waters et al \(1998\)](#) proposed a scenario for mixed chemistry in which a presently carbon-rich star may retain in its outer layers the circumstellar oxygen-rich gas due to an earlier phase of mass loss. This scenario can then account for both carbon-rich (PAH emission) and oxygen-rich (silicate emission) signatures. Using SOFIA infrared imager observations combined with 3D photoionization and dust radiative transfer modeling, [Guzman-Ramirez et al. \(2015\)](#) also demonstrated that oxygen-rich (silicate) dust occurs in the outer regions of the planetary nebula BD +30° 3639 while the carbon-rich material (PAHs) is located in the inner parts. These earlier studies suggest the emergence of mixed chemistry possibly caused by dredge-up of carbon from inner regions of the central star towards the end of the AGB stage.

The absorption due to silicates at 9.7 and 18 μm has been observed in 7 sources. The spectral types of all these sources are not known due to the possibility of their photospheres being heavily enshrouded by circumstellar shells. [García-Lario and Perea Calderón \(2003\)](#) suggested an increased thickness of the circumstellar shell responsible for the absorption features in oxygen-rich sources.

The broad 11 μm feature usually attributed to SiC has been observed in IRAS 08005-2356, IRAS 11339-6004, IRAS 14325-6428, IRAS 14341-6211, IRAS 16494-3930 and IRAS 17359-2902. It may be noted that these sources do not show PAH emissions. It is generally believed that SiC emission features are observed in sources with very thick dust shells formed from carbon-based dust grains. [García-Lario and Perea Calderón \(2003\)](#) attributed the observed increase in the strength of the SiC feature in carbon stars to the increased mass-loss rate during the AGB phase of the stars. [Speck et al. \(2005\)](#) argued that the change in the appearance of the 11 μm feature is a result of self-absorption from the thick dust shells.

In the longer wavelength region, among the six sources in this category, two sources show 30 μm feature; and the two other sources do not show 30 μm feature but show crystalline olivines.

Among the 3 objects that are categorised as showing featureless spectra, the sources IRAS 19454+2920 & IRAS 20259+4206 show narrow absorption line of the carbon based molecule, C_2H_2 at 13.7 μm suggesting their advanced stage of evolution towards a carbon-rich star; in addition to the featureless thermal continuum due to dust. On the basis of the observed featureless thermal emission from the circumstellar envelope and a weak Rayleigh-Jeans tail at the shorter wavelengths due to the central star, it may be conjectured that objects displaying such spectral characteristics may be relatively young PAGB stars evolving beyond the heavily enshrouded OH/IR stars (Waelkens and Waters (2003)).

The carrier candidates for the 21 and 30 μm feature are still being debated. The candidates for the 21 μm feature include TiC (von Helden et al. (2000)), doped SiC dust (Speck and Hofmeister (2004)), FeO (Posch et al. (2004)) and PAH molecules (Justtanont et al. (1996)). Goebel and Moseley (1985) suggested solid magnesium sulphide (MgS) as the possible carrier for the 30 μm feature, while Duley (2000) suggested carbon-based linear molecules with specific side groups.

For the purpose of analysing the correlations, equivalent widths (EWs) of the most prominent mid-infrared PAH features, namely, those at 6.2, 7.7 & 11.2 μm , were derived using the Spectroscopic Modeling Analysis and Reduction Tool (SMART). Table 2 lists the EWs for all objects that showed PAH features. The table also lists the peak positions of the three features for each object. EWs of the three PAH features considered here were determined using the procedures adopted by Hony et al. (2001), Peeters et al. (2002) and Peeters et al. (2017). In addition to the global continuum as shown in Fig 2a, the local continuum around the 5-12 μm region is enhanced by broad plateaus around 5-7 μm , 7-8 μm (8 μm bump) and 10-12 μm (see Peeters et al. (2017) and the references therein). These plateaus are typically shown by asterisks in Fig 2a (see class 1a, 1c, 2b in top three panels). The pivotal points defining the plateau continua were fitted by second or third order polynomial and subtracted from the raw spectra. The resulting continuum-subtracted spectra around 6.2, 7.7 and 11.2 μm were fitted suitably by single/multi Gaussian profiles (using LINE FIT task in SMART) to account for the PAH emission features. In most cases, spectral decomposition using two Gaussian was required to account for blended components of PAH emission at 7 and 11 μm regions, while the 6.2 μm feature required single Gaussian in

6 objects, two in 12 and three Gaussians in 3 objects. Figure 2b shows continuum-subtracted spectra of 3 objects (of Classes 1a, 1c and 2b) for which Gaussian decomposition is illustrated. In the literature several methods had been used to extract the intensity or EWs of the PAH features (e.g. Drude profiles (Smith et al. (2007)), Lorentzian (Galliano et al. (2008)) and Gaussian (Uchida et al. (2000), Hony et al. (2001), Peeters et al. (2002), Blasberger et al. (2017) and Peeters et al. (2017))). In a recent study Peeters et al. (2017) concluded that for a large sample of objects PAH correlations are independent of the method adopted. The earlier studies suggested that the line fluxes were only marginally affected by the choice of the profile while they depend more on the choice of the continuum. Further, the line centre determination does not critically depend upon the choice of profile (for e.g. Blasberger et al. (2017)). The errors in the EW of the PAH features (see Table 2) were estimated using the relation,

$$\sigma_T^2(W) = M. \left(\frac{h_\lambda}{S/N} \right)^2 \cdot \frac{\tilde{F}_j}{\tilde{F}_c} + \left[\frac{\sigma(\tilde{F}_c)}{\tilde{F}_c} \cdot (\Delta\lambda - W) \right]^2 \quad (1)$$

from Chalabaev and Maillard (1983), where h_λ is the spectral resolution per pixel, M is the number of pixels, S/N the signal to noise ratio, $\frac{\tilde{F}_j}{\tilde{F}_c}$ represent the ratio of the measured flux over the continuum summed over the number of pixels and $\sigma(\tilde{F}_c)$ represent the uncertainty in the continuum, $\Delta\lambda = \lambda_1 - \lambda_2$ is the wavelength range covered by the feature and W represents the EW.

4 MODELING OF SEDS:

The SEDs of the sample stars constructed from archival photometric data, were modeled using the software DUSTY (Ivezic et al. (1999)). The input parameters for each object consist of stellar photospheric temperature (T_*), temperature of the inner region of the dust shell (T_d), composition of the dust grains, density distribution and the optical depth at 0.55 μm ($\tau_{0.55}$). The composition of the dust considered here for the individual sources is based on the observed spectral features in their *Spitzer* IRS spectra. The parameters that are fixed are T_* , dust particle size limits and size distribution index; and density distribution. The variable parameters are T_d , composition of dust grains (for continuum we mainly used either graphite (Gr) or amorphous carbon (AmC)), optical depth at 0.55 μm ($\tau_{0.55}$). The code solves the radiative transfer problem for a source embedded in a spherically symmetric

dusty envelope. The important output parameters of the code are the total flux as a function of wavelength, the inner shell radius r_1 , the ratio of inner shell radius and the radius of central source, r_1/r_c , terminal velocity and upper limit of the mass of the source. The model also gives an estimate of the total mass loss rate ($dM_{gas+dust}/dt=\dot{M}$) for envelope expansion caused by radiatively driven winds with an uncertainty of 30 %. [Meixner et al. \(1997\)](#) and [Mishra et al. \(2016\)](#) used axisymmetric models to infer mass-loss rates. We find a good agreement with these models for some sources that are common in our sample.

The model fluxes are compared with the observed values, by normalising with the flux at either 2 μm (K band) or at 9 μm band (of MSX or *AKARI* or IRAC) depending upon the distribution of observed data points in the infrared range. T_* was taken from [Cox \(2000\)](#) and [Lang \(1999\)](#) for objects whose spectral types are identified. For all the other objects (25 in number) whose spectral types are not available, we have estimated T_* from model best fits. For a majority of programme objects, the best fit degeneracy is very minimal and can be gauged by the uncertainty on T_d ($< 5\%$) and $\tau_{0.55}$ (about 10 %), grain composition that contributes for the continuum ($< 10\%$). A criterion for the best fit was chosen as, $\chi^2 = \sum_i [(F_{O_i} - F_{M_i})^2 / F_{M_i}] \leq 10^{-12}$, where \sum_i indicates summing over all the data points ($i=1$ to n , n being the number of data points for a particular source) and F_{O_i} and F_{M_i} are the observed and model fluxes at i^{th} data point respectively. For each object, several models were generated by tweaking the variable parameters (T_d , grain composition and $\tau_{0.55}$) and we chose the best model as determined by the chi-square criterion as well as by visual inspection. Barring a few, for most sources in our sample, the limit on χ^2 had resulted in (visually) reasonably good fits, except for a few sources. It may be noted that the spectral class differences in some of the objects that are common in SIMBAD and [Suárez et al. \(2006\)](#) did not alter the model-derived parameters by more than 10%.

In general, the double-humped SEDs of PAGB stars indicate detached dust shells, in contrast with the AGB stars ([Venkata Raman and Anandarao \(2008\)](#)). For the purpose of modeling, we have divided our sample stars into two categories, based on their IRS spectra: (i) those that show clearly the PAH features in the 6 - 15 μm region (ii) those showing no PAH feature at all. Strong & weak/blended PAHs were modeled using a double shell geometry because PAH alone could not account for the continuum emission on either side of the 5 - 15 μm region, while the sources with silicate in emission/absorption, and broad 11 μm feature were modeled using single shell geometry. A SED model using a single dust shell with graphite, amorphous carbon, SiC and silicate dust grains or a combination of these, as

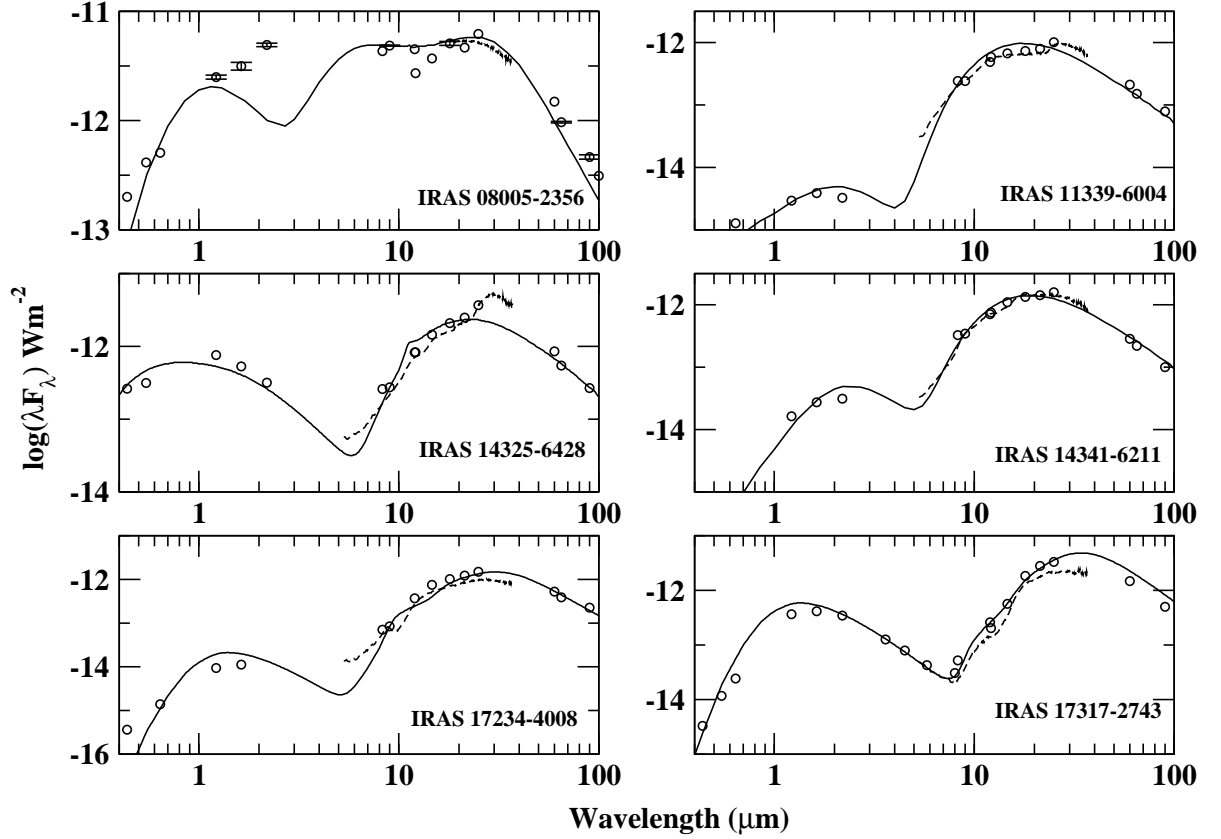


Figure 3. Model SEDs with single spherical shells using DUSTY (solid line) for a few PAGB sources compared with observed data from literature (open circles). The *Spitzer* IRS spectra (dashed line) are shown for comparison. Being in the log scale the error bars are of the point size.

the case may be, better represented the circumstellar sources without PAH emissions. SED models using two shells better modeled strong, weak/blended PAH and mixed chemistry sources, with an inner shell of PAH and an outer shell containing graphite or amorphous carbon or silicate dust grains. The optical constants for the PAH were provided externally into DUSTY while the other dust grains used here are in-built with DUSTY. A modified MRN (Mathis et al. (1977)) dust size distribution was assumed with an exponent of 3.5 with minimum and maximum dust grain sizes of 0.005 and 0.25 μm respectively. A radiatively driven wind model was chosen for the dust shell with density distribution of type 3 (see Ivezić and Elitzur (1995)), in which the envelope expansion is owing to the radiation pressure on dust grain particles (see Ivezić and Elitzur (1997)). Table 3 shows the list of

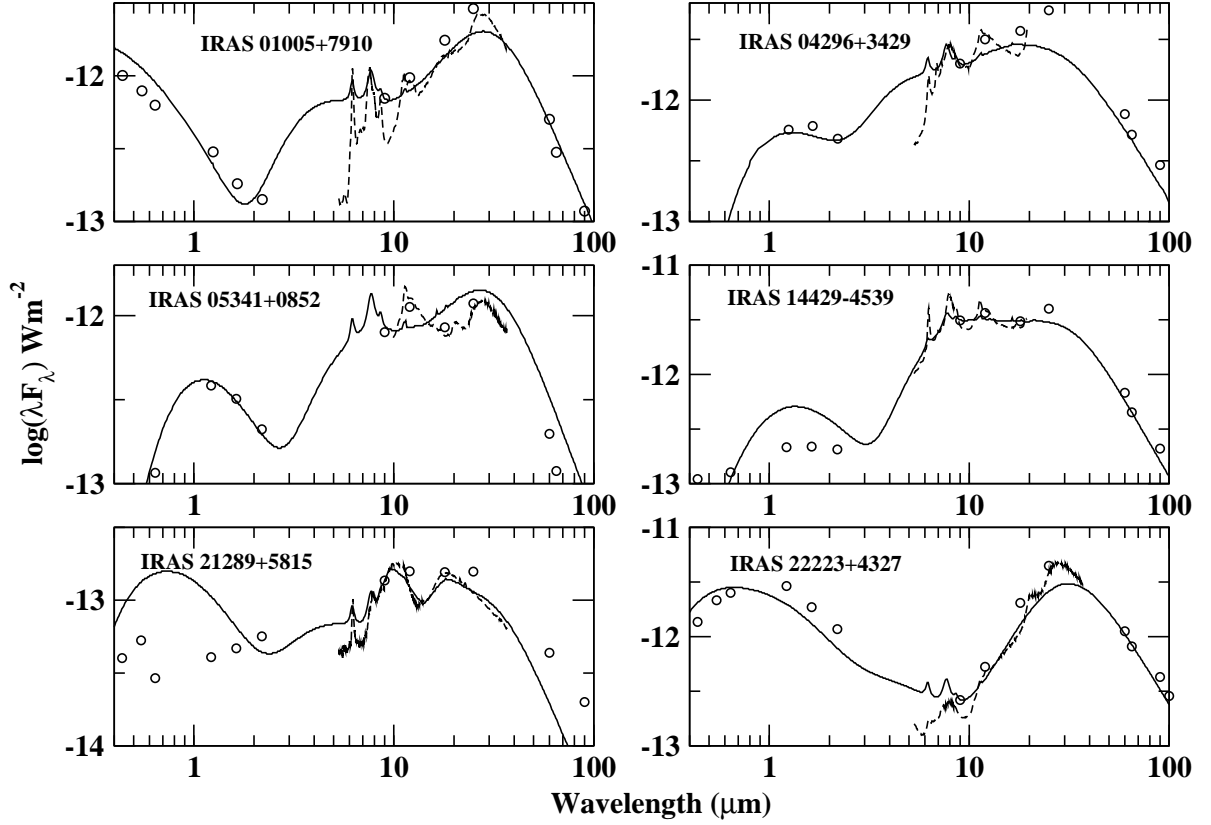


Figure 4. Model SEDs with two spherical shells using DUSTY (solid line) for a few PAGB sources that showed strong PAH emissions compared with observed data from literature (open circles). The *Spitzer* IRS spectra (dashed line) are shown for comparison. Being in the log scale the error bars are of the point size.

single-shelled PAGB sources along with model-derived photospheric and circumstellar shell parameters, namely, T_* , T_d , \dot{M} , $\tau_{0.55}$, r_1 , r_1/r_c and the grain composition (Gr is for graphite and AmC for amorphous carbon and Sil for silicate grains with the portion in 1 given in parentheses). Also listed in the Table 3 are the dust mass loss rates \dot{M}_d using the following empirical relation by [Lagadec et al. \(2008\)](#),

$$\log(\dot{M}_d) = -9.58 + 0.26(K_s - [11]) + 0.05(K_s - [11])^2 - 0.0053(K_s - [11])^3 \quad (2)$$

where K_s and [11] are the magnitudes of the sources in the 2MASS K band and VISIR PAH2 filter ($\lambda_c = 11.25 \mu\text{m}$, $\Delta\lambda = 0.59 \mu\text{m}$) respectively. The dust mass loss rates obtained from

infrared colors were found to be in the range between 10^{-8} to $10^{-10} M_{\odot}\text{yr}^{-1}$ agreeing well with the results of [Lagadec et al. \(2008\)](#). It is clear from the table that the grain composition for all the sample stars is carbonaceous dust (either graphite or amorphous carbon or a combination of the two). This result, however, does not fall in line with the finding of [Cerrigone et al. \(2009\)](#), whose sample showed only 25% having carbon rich envelopes. Figure 3 shows typical model fits for the PAGB stars with single shell. Photometric observations as well as *Spitzer* IRS spectra are overplotted for comparison.

For those sources (27 in number) in which the *Spitzer* IRS spectra showed strong PAH emissions, we have used two spherical shells (instead of one used before) for the SED modeling using DUSTY. The first or inner shell contains predominantly neutral or ionised PAH and the second, outer shell contains any of the common dust grains (amorphous carbon/silicate/graphite). The ratio of the 6.2 or 7.6 μm PAH over 11.2 μm feature can be used as a measure of the ionization fraction of the PAHs, because the ionized PAHs emit more strongly in the 6.2 and 7.6 μm bands while the 11.2 μm band is stronger in neutral PAHs. This ratio may be estimated from *Spitzer* mid-IR spectra and whether the PAHs are neutral or ionized may be ascertained in a given source. The optical properties obtained from [Li and Draine \(2001\)](#) for neutral and ionised PAHs with grain size of 0.01 μm was used as external input to the DUSTY software. The density distribution falling off as r^{-2} was used for both the dust shells. Fig 4 shows typical model fits with double shells for the PAGB candidates. Table 4 show the list of these PAGB sources along with the derived photospheric and circumstellar shell parameters, T_* , T_d , ionised state of PAH in the first sphere, r_1 , r_1/r_c for both the shells and the grain composition in the dust shell 2. It is assumed that PAH and dust exist in two separate shells with the former closer to the star than the latter. The PAH emissions may be from regions very close to the edge of the photo-dissociation regions.

We note here that it may be quite reasonable to assume that PAH molecules exist in a separate shell closer to the star because they require soft-UV radiation for excitation. Further, it is possible that the PAH shell could form close to the central star during the most recent PAGB mass loss episode where the outer layer of the central star is enriched with carbon rich materials due to a thermal pulse. As mentioned earlier, [Waters et al. \(1998\)](#) used similar arguments for explaining the observed the oxygen and carbon rich signatures in the binary system of Red Rectangle. As mentioned earlier, [Guzman-Ramirez et al. \(2015\)](#) suggested that in the planetray nebula BD +30° 3639, the carbonaceous dust (PAH) exists in the inner regions while the oxygen-rich dust (silicates) in the outer regions of the nebula.

5 RESULTS AND DISCUSSION:

5.1 Dust formation distance

The SED modeling reveals a few interesting, physically viable relationships between various derived parameters. Fig 5 shows the plot between inner dust temperature and the inner radius of the dust shell for all the stars in our sample. In the case of objects showing PAH spectra, the inner radii of both the PAH and dust shells are shown in the figure. The plot shows that as the dust temperature increases the radius of the inner shell decreases. This simply implies that the dust gets cooler as it is located farther from the star. It may be inferred from the figure that the inner radius of the dust shell corresponding to a typical condensation temperature for (silicate) dust grains, $T_c \sim 1600\text{K}$, turns out to be $\sim 3.5 \times 10^{12}$ m. It indicates that the dust formation distance from the stellar photosphere is typically a few stellar radii. It was argued by [Woitke et al. \(1996\)](#) & [Sedlmayr and Winters \(2000\)](#) that for pulsationally driven mass loss to be most efficient, the dust formation should occur at a few stellar radii (R_*).

Fig 6 shows the plot of T_* as a function of ratio r_1/r_c . The plot indicates that the ratio increases with T_* . As the photospheric temperature increases the star emits copious amount of UV photons that destroy the dust and hence the dust can survive only at distances far off from the star. This explains the positive correlation between the two parameters. This is in line with the above argument on minimum distance of dust formation.

5.2 Trends in the mass-loss rates

The PAGB mass loss mechanisms are not well-understood and still being debated. Initially a continued or extended superwind phase until the central star attains a certain temperature was assumed to explain the PAGB mass loss rates ([Schoenberner \(1983\)](#)). However, very recently [Hrivnak et al. \(2015\)](#) attributed the variation in the PAGB light curve to pulsations that levitate the circumstellar envelopes to sufficient heights leading to dust formation. As the central stars evolve and the temperature increases, radiation driven winds facilitate the mass loss process ([Vassiliadis and Wood \(1994\)](#)). The mass loss rates obtained from the model for our sample of PAGB stars showed expected trends with the other model-derived parameters. Despite considerable scatter, especially for optically thin cases ($\tau_{0.55} \leq 1.0$), one may infer from Fig 7 an increasing trend in mass loss rate with optical depth at $0.55 \mu\text{m}$. During the mass loss process, the dust shell remains initially optically thin, allowing the

radiation from the central star to escape out. But as the mass loss increases, the optical depth increases leading to the formation of thick circumstellar shell resulting in formation of dust that completely blocks the radiation escaping the central star. These are physically expected results and hence the plots serve as a validation of circumstellar dust shell properties. Fig 8 shows the tendency of decreasing mass loss rate with increasing inner dust temperature in line with the above arguments. Since most of the dust grains (silicates and graphites) condense at approximately at the same temperature around 1500 K (Salpeter (1977)), a strong dependence on the effective temperature (T_*) is expected. An increase in the stellar temperature moves the dust nucleation region outward and hence towards lower densities which leads to an ineffective coupling between the gas and dust thereby decreasing the mass-loss rates (Lamers and Cassinelli (1999)). Also, as T_d increases the dust shells tend to be located closer to the central star where the dust is destroyed, leading to a low mass loss rate.

The color [K-12] is often considered as an indicator of mass loss in AGB/PAGB stars (Le Bertre and Winters (1998)). Anandarao et al. (1993) proposed that the color index [25-2] as a better tool for representing mass loss rate in AGB stars. Fig. 9 shows the plot of the total mass loss rates for all those PAGB stars that have single dust shells with [25-2] & [K-12]. Also included in the figure are the sample of AGB stars from our previous work (Venkata Raman and Anandarao (2008)). The figure indicates that the mass loss rate does not cease completely towards the end of the AGB phase but extends beyond and towards the PAGB phase. The PAGB mass loss rate was found to be much higher than that during the AGB phase. Figure 9 also shows the mass loss rates for some PAGB stars (common with our sample) determined from the observed CO rotational line profiles by several authors, namely Woodsworth et al. (1990), Likkell et al. (1991), Omont et al. (1993), Hrivnak and Kwok (1999), Bujarrabal et al. (2001), Hoogzaad et al. (2002) and Hrivnak and Bieging (2005). One can see a good agreement between the model values and those determined by observations. Fig 10 shows the plot of dust mass loss rates as a function of the colors [25-2] and [K-12], indicating a similar trend as the total mass loss rate. Fig 9 shows two distinct regions: an initial positive correlation of mass-loss rate with [K-12] & [25-2] colors due to the initiation of the superwind towards the end of AGB phase, and the continued constant high mass loss rates during the PAGB stage possibly due to the pulsation and radiatively driven winds from the central star. Recently, de Vries et al. (2014) suggested an intense mass loss due to 'hyperwinds' that occur between the superwind and the PPNe phase to explain the high mass loss rates during the PAGB phase. It is, however, not clear as to

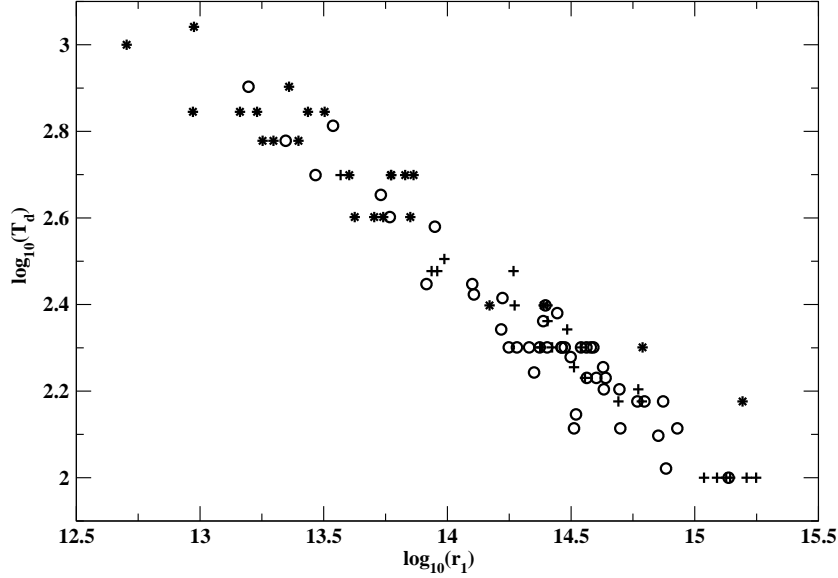


Figure 5. Plot of dust temperature T_d versus the inner dust shell radius r_1 (in m) for the PAGB stars (open circles) obtained from DUSTY SED models with single shell irradiated by radiatively driven winds. The asterisk and pluses represent the sphere 1 (PAH) and sphere 2 for PAGB candidates modeled with a double circumstellar shell geometry.

what causes this hyperwind, or for that matter, the superwind itself. [de Vries et al. \(2015\)](#) also suggested the presence of crystalline forsterite (Mg_2SiO_4) as a signature for massive AGB stars. Based on the variation in the circumstellar nebular conditions and the observed variations in the spectral features, [García-Lario and Perea Calderón \(2003\)](#) had proposed an evolutionary scheme for both oxygen and carbon rich sources in transition from AGB to PN phase. About 15 stars in our sample show the presence of crystalline forsterite at $33.6 \mu\text{m}$ feature suggesting possibly their massive nature. These massive AGB stars cannot lose their entire envelope during the superwind phase alone. So the intense mass loss should continue beyond the superwind phase before becoming a PN, thus explaining our SED model results. [Hrivnak and Biegging \(2005\)](#) had suggested an intense mass loss during the PAGB phase responsible for the steeper density law for fitting their observed CO rotational line profiles.

5.3 Trends in PAH modes with the evolution:

Here we examine the trends in the strength of the PAH emission modes with the stellar effective temperature T_* . The T_* is used to represent the evolutionary stage of the sources considered in the present study; higher the value, the more advanced is the evolution of the

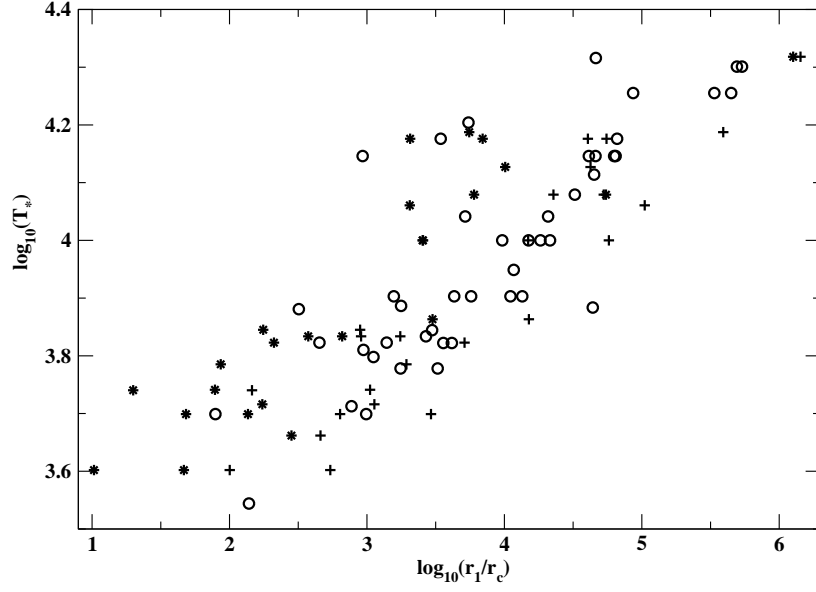


Figure 6. Plot of central source temperature T_* versus the ratio of inner dust shell radius r_1 and the central source radius r_c for PAGB stars (open circles) obtained from DUSTY SED models with single shell irradiated by radiatively driven winds. The asterisks and pluses represent the sphere 1 (PAH) and sphere 2 for PAGB candidates modeled with a double shell geometry.

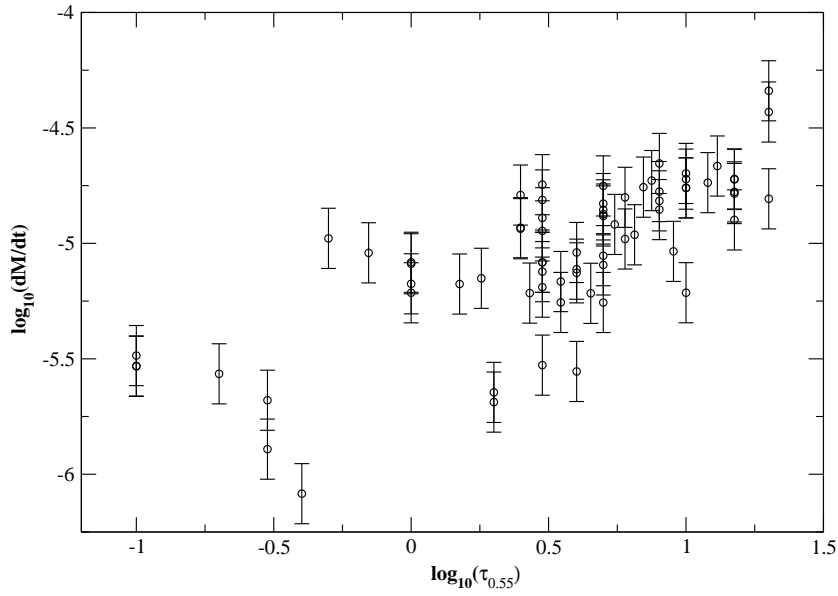


Figure 7. Plot of total mass loss rate dM/dt versus the optical depth at $0.55\mu\text{m}$ $\tau_{0.55}$ for PAGB stars.

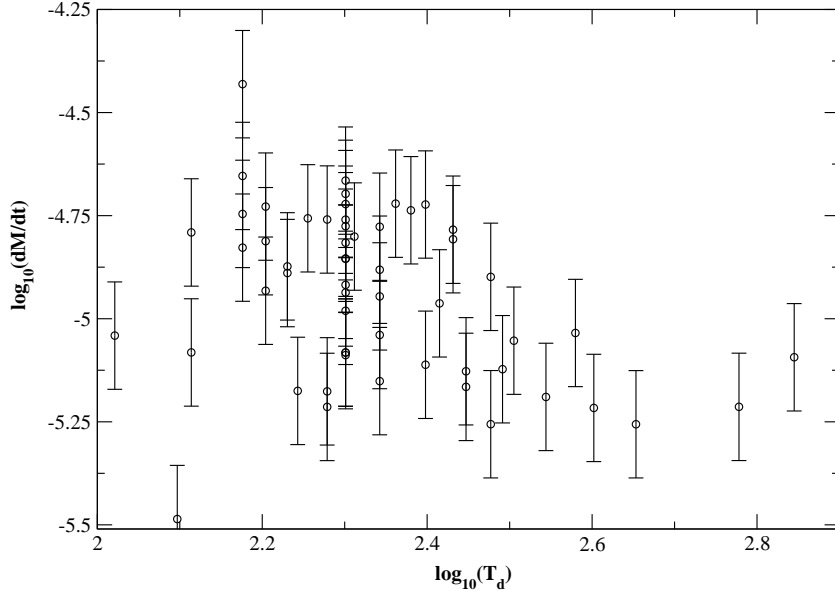


Figure 8. Plot of total mass loss rate dM/dt versus the dust temperature T_d for PAGB stars.

source. Interesting correlations were obtained between the strengths of the PAH spectral features with the physical and circumstellar parameters of the PAGB candidates by [Peeters et al. \(2002\)](#), [Sloan et al. \(2005\)](#), [Bernard-Salas et al. \(2009\)](#) and [Hony et al. \(2001\)](#). In this section, we examine the present sample of PAGB objects for such possible correlations with stellar temperature and other parameters that characterize circumstellar envelope.

Firstly, we examined the correlation between intensity ratio $I(7.7)/I(11.2)$ and $I(6.2)/I(11.2)$. Each of these ratios is known to indicate the ionization fraction in PAH molecules ([Galliano et al. \(2008\)](#)). Fig 11 shows a plot of these intensity ratios indicating a positive correlation, a trend that was earlier shown by [Cerrigone et al. \(2009\)](#).

We have also studied the relative dominance of C-C stretching and C-H in-plane bending modes (e.g. $7.7 \mu\text{m}$) and C-H out-of-plane (e.g. $11.2 \mu\text{m}$) modes as the stars evolve. It may be noted that we have used the equivalent width (EW) as the measure of the strength of the PAH feature instead of the feature intensity used by other authors (e.g. [Cerrigone et al. \(2009\)](#), [Zhang et al. \(2010\)](#)). We have found that using EW yielded essentially the same results as using intensity of spectral features. Fig 12 and 13 show the ratio of the EWs of the PAH features $[7.7]/[11.2]$ versus T_* and radius of the central source r_c respectively. The PAH feature at $7.7 \mu\text{m}$ represents the C-C stretching and C-H in-plane bending modes and

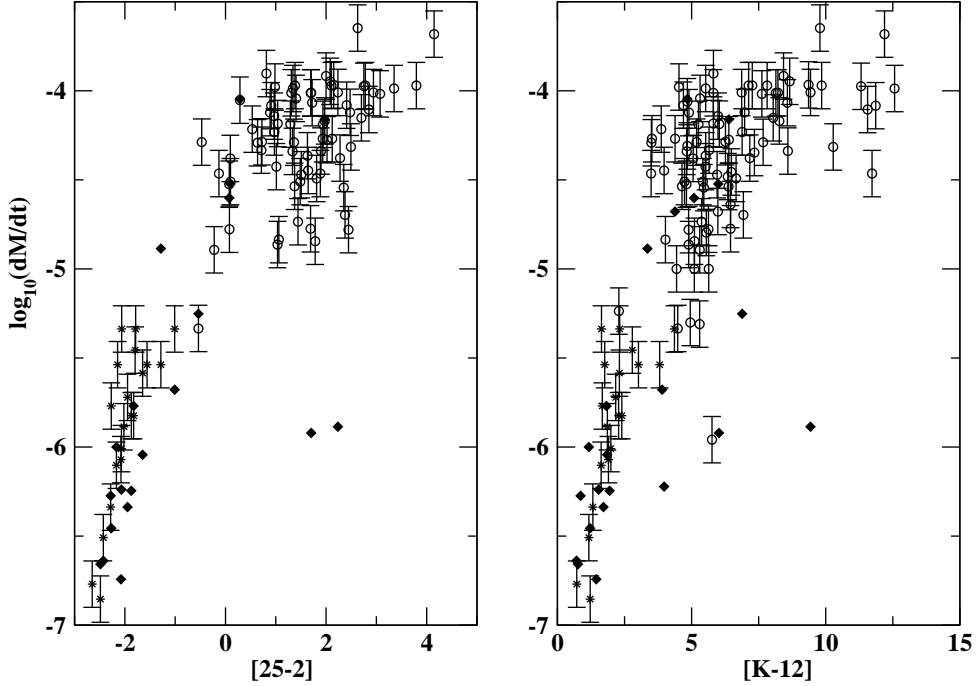


Figure 9. Plot of the total mass loss rate obtained from DUSTY with the mass loss index $[25-2]$ & $[K-12]$ for AGB (asterisks) and PAGB stars (open circles). The mass loss rates derived from the observed rotational transitions of CO at mm wavelengths for some of the AGB and PAGB stars in our sample (filled diamonds) are also shown for comparison.

the $11.2 \mu\text{m}$ feature represents the solo C-H out-of-plane bending modes. One may notice a tendency of increasing ratio with T_* indicating the dominance of C-C stretching and C-H in-plane bending modes as the objects evolve; while a decreasing tendency may be noticed with r_c . As mentioned earlier, one may also conclude from this plot that stars showing ratio $[7.7/11.2] > 1$ have higher fraction of ionised PAHs than those with lower ratio.

In their study of a few PAGB candidates, [Zhang et al. \(2010\)](#) showed that the ratio $[12.6/11.2]$ tends to decrease with the central star temperature, indicating that the solo C-H modes at $11.2 \mu\text{m}$ become more and more predominant over the duo- or trio- or quarto-modes at $12-13 \mu\text{m}$. This is suggestive of the possibility that the solo C-H out-of-plane bending modes get stronger as the star evolves to PNe ([Kwok \(2004\)](#)). We also found in the present sample that the ratio indicated a decreasing trend with T_* (not shown here). The ratio is less than 1 for nearly all the sources that showed PAH bands suggesting that the solo-modes dominate over the duo and trio modes. Our result is in agreement with [Zhang](#)

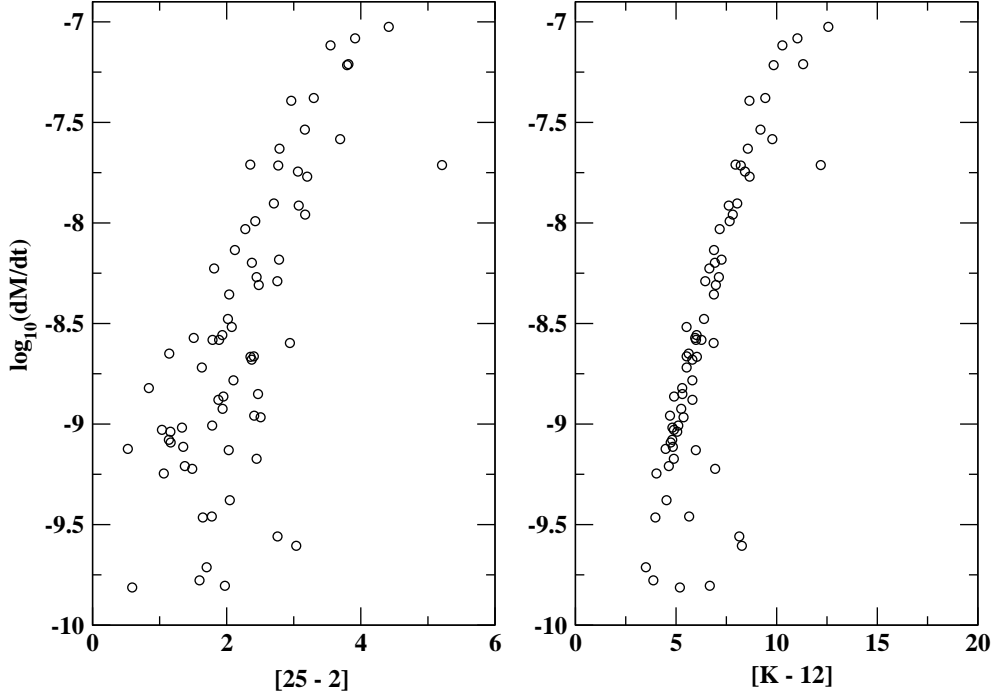


Figure 10. Plot of the dust mass loss rate obtained using the relation from [Lagadec et al. \(2008\)](#) with the mass loss index $[25-2]$ & $[K-12]$ for the sample PAGB stars (open circles).

[et al. \(2010\)](#). In most cases of PNe in their sample, [Hony et al \(2001\)](#) found that the ratio as a function of hard radiation field remained less than 1.

We have also seen if there is a trend between the central source temperature and the plateau region $16-20 \mu\text{m}$ representing the blended features of in-plane or out-of-plane C-C-C bending modes normalised with the $11.2 \mu\text{m}$ solo band. A decreasing trend of the mode with T_* was noticed (not shown here).

[Sloan et al. \(2007\)](#) showed that the peak wavelength of the $11.2 \mu\text{m}$ feature changes with T_* for a small sample of carbon stars. We verified this result with our sample. Fig 14 shows the plot of the peak wavelengths of the 6.2 , 7.7 and $11.2 \mu\text{m}$ features with T_* (see Table 2). One may notice, in general, a shift towards the shorter wavelengths with increasing T_* , up to a value of 10^4 K in agreement with [Zhang et al. \(2010\)](#). [Sloan et al. \(2007\)](#) assume that PAH clusters are embedded in a matrix of aliphatic groups. When such hydrogenated amorphous carbon (HAC) material is exposed to hard radiations, the aliphatic bonds break

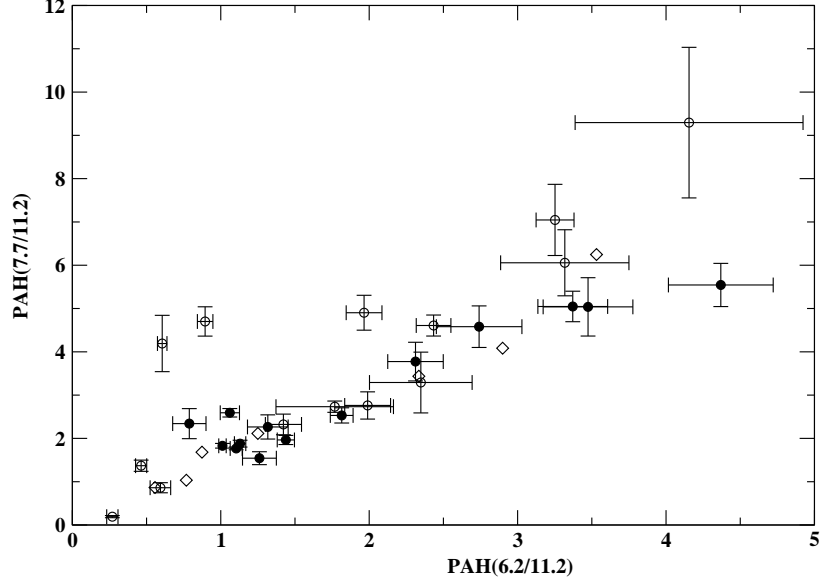


Figure 11. Plot of PAH mode flux ratio $[7.7]/[11.2]$ vs $[6.2]/[11.2]$ for PAGB stars. The open circles represent the PAGB stars in our sample while the filled circles represent PNe in the Large Magellanic cloud (LMC) and Small Magellanic cloud (SMC) and the open diamonds represent the same in our milky way galaxy obtained from Bernard-Salas et al. (2009) are shown for comparison.

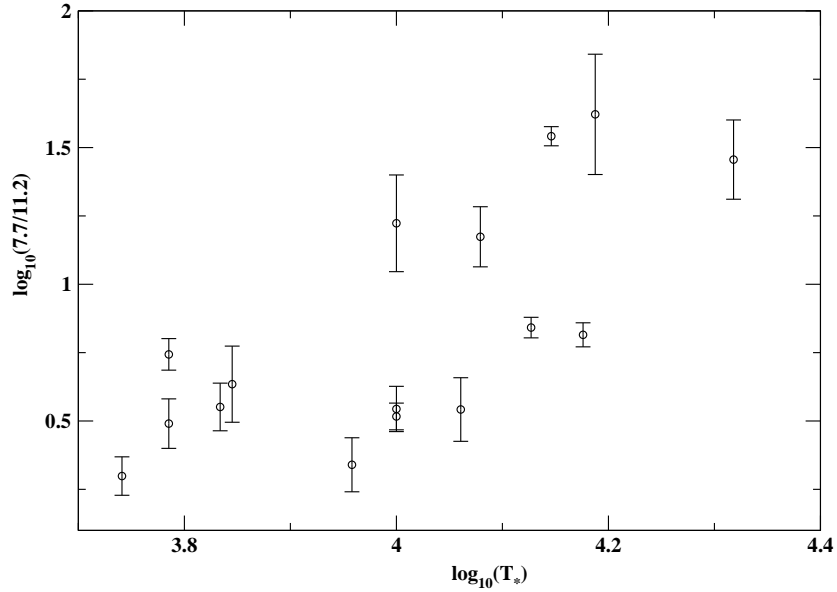


Figure 12. Plot of PAH mode ratio $EW[7.7]/EW[11.2]$ versus the effective temperature T_* for PAGB stars.

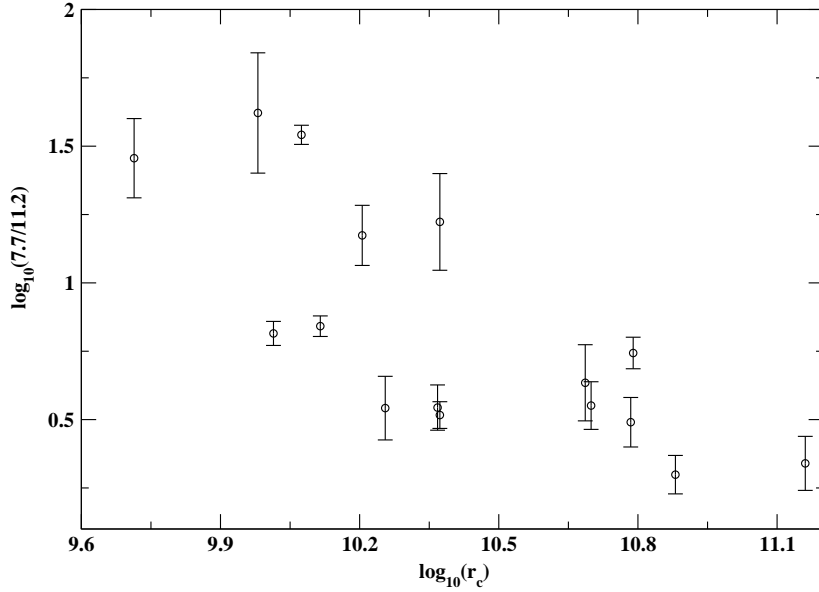


Figure 13. Plot of PAH mode ratio $EW[7.7]/EW[11.2]$ versus the radius of the central source r_c for PAGB stars.

down progressively leading to the positional shifts of PAH features (for details see [Sloan et al. \(2007\)](#)).

6 IDENTIFICATION OF TRANSITION OBJECTS

The transition process from the post-AGB to PNe phase still remains elusive in stellar evolution. After the termination of the high AGB mass loss, the circumstellar envelopes expand and cool, and the effective temperature of the central star increases to ionize the circumstellar material towards the end of the post-AGB phase ([Kwok and Feldman \(1981\)](#), [Kwok and Bignell \(1984\)](#)). Mid-IR fine structure lines suffer less dust extinction compared to the optical and UV emission lines and hence are easier to detect. However not all the PAGB objects show these emission lines that indicate their transition nature; a possible explanation is in order. The morphologies of PAGB dust shells are believed to be predominantly axisymmetric ([Ueta et al. \(2000\)](#)) that interact with the PAGB winds to form aspherical PN shells. Mid-infrared imaging of PAGB sources show a central dust torus around the central source ([Ueta et al. \(2001\)](#)). The mid-IR morphologies of the circumstellar shell are characterized into two groups namely toroidal and core/elliptical ([Meixner et al. \(1999\)](#)). The toroidal dust shells have very low optical depth and the star light can scatter in all directions. In

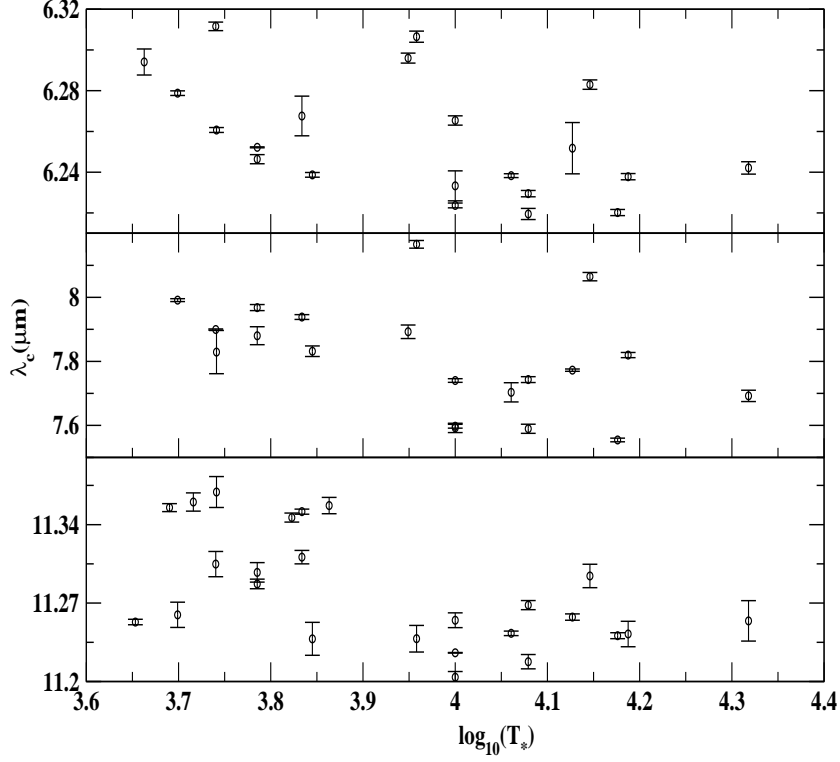


Figure 14. Plot of the peak wavelength of the PAH feature at 6.2, 7.7 & 11.2 μm versus the photospheric temperature T_* for PAGB stars.

the case of elliptical mid-IR shells the optical depth is high and the starlight can escape only through the bi-cone opening of the dust shell making bipolar nebulosities. The fine structure emission lines are believed to arise from the irradiated central torus atmospheres. In order to observe these lines, the inclination of the source and the optical depth along the line of sight play a crucial role. If the source is viewed pole-on then the line of sight optical depth is the highest from the circumstellar shells and makes the detection difficult. When observed edge-on one may view the interaction of the fast winds with the dense equatorial torus. Hence the detection of these lines depends on the morphology and inclination of the source.

Figure 15 represents *Spitzer* IRS spectra of transition objects with hot cores ionizing the circumstellar matter, thereby making a transition from PAGB to PNe phase, showing low and high excitation fine structure lines. There are around 31 objects in the sample which may be termed as hot objects having $T_* \geq 10^4$ K but only 9 of these show fine

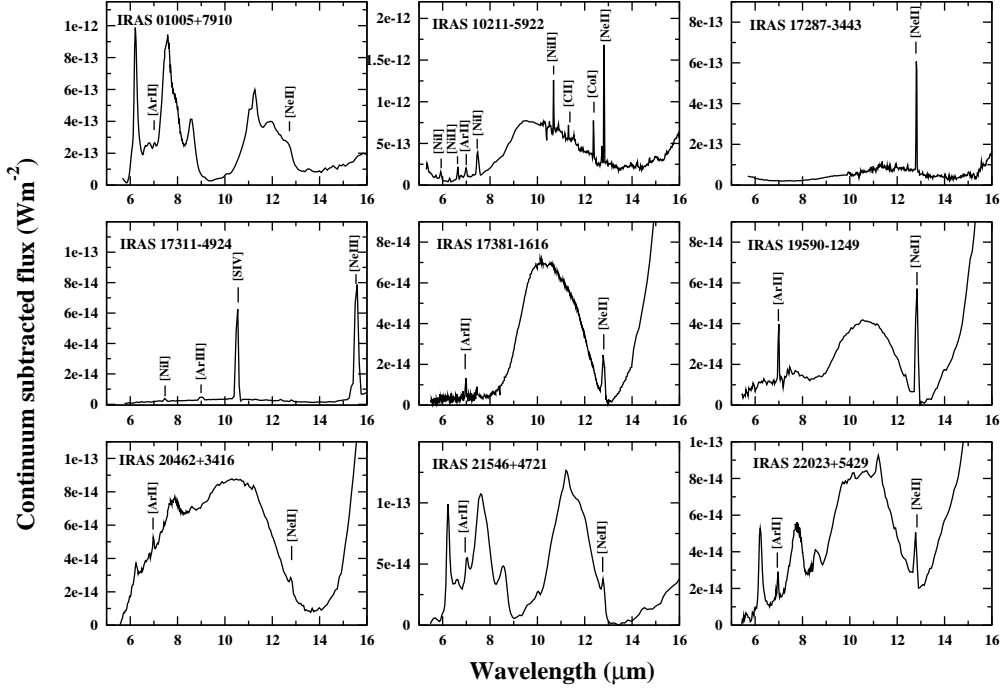


Figure 15. Transition objects from our sample showing prominent low and high excitation fine structure lines

structure lines of Ne. The IRS spectra of the PAGB candidate IRAS 01005+7910 IRAS 21546+4721 and IRAS 22023+5429 showed PAH emission in addition to [NeII]. Among the other PAGB candidates showing transition behavior, IRAS 10211-5922, IRAS 17381-1616 and IRAS 19590-1249 showed silicate in emission. The source IRAS 10211-5922 shows [NiI], [NiII], [ArII], [CoI] and [CII] in addition to the [NeII] line, thereby suggesting its advanced stage of evolution among the other candidates. Also, IRAS 17287-3443 and IRAS 17311-4924 show peculiar dust properties in addition to the fine structure lines. IRAS 17311-4924 shows high excitation lines of [ArIII], [SIV] and [NeIII] in addition to the [NiI] lines. It also shows faint emission of [NeII] line at relatively lower S/N. Further, it shows a rising mid-infrared continuum (near the [SIV] line) possibly due to VSGs that can survive close to the hot source (Lebouteiller et al. (2007)). In the light of these fine structure line emissions and the contribution due to VSGs, IRAS 17311-4924 might be a high excitation transition object. The sources IRAS 20462+3416 and IRAS 22023+5429 are mixed chemistry objects with [NeII] emission. As argued above, the reason for fewer candidates showing [NeII] emission could be due to orientation effect and deeply embedded nature of the elliptical dust shells.

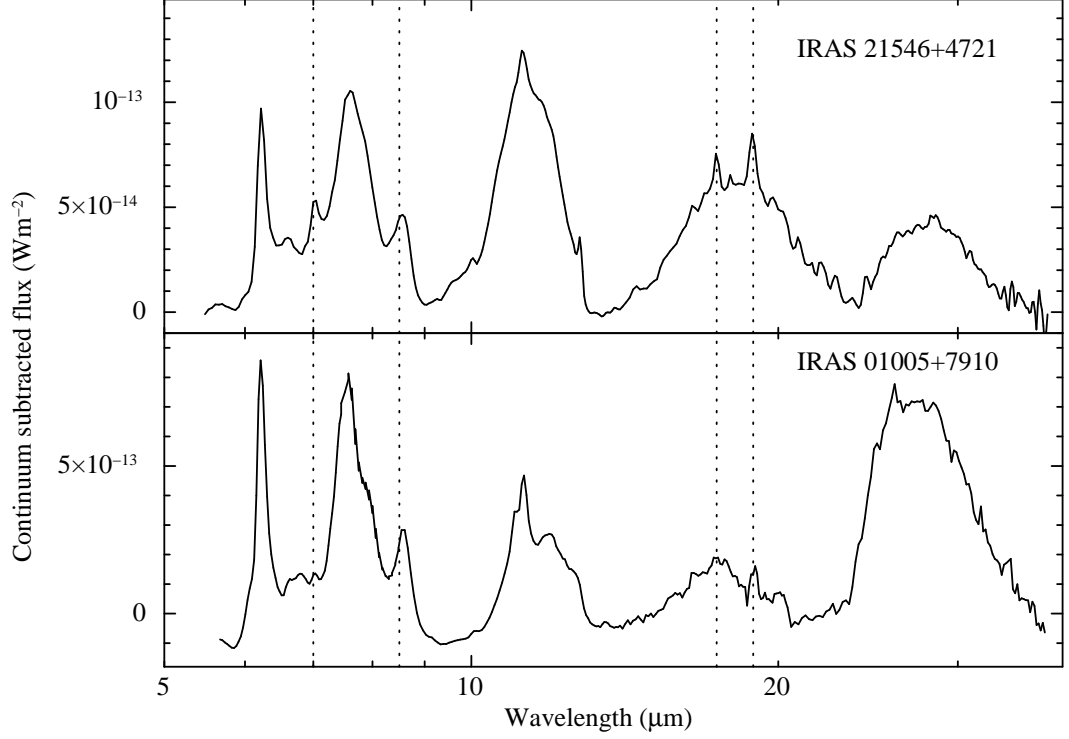


Figure 16. *Spitzer* IRS spectra of PAGB candidates IRAS 21546+4721 and IRAS 01005+7910 showing vibrational modes of C_{60} fullerene

Our SED model of sources with hot central temperatures also shows large $\tau_{0.55}$ values. Even with the uncertainty associated with model $\tau_{0.55}$ values, the trend is compelling: those that showed [NeII] line have much lower $\tau_{0.55}$ values with an exception of IRAS 17287-3443 compared to those that did not.

7 DETECTION OF FULLERENE IN IRAS 21546+4721

Fullerene molecules (C_{60}) are large molecules made of carbon hexagons and pentagons that are organised in the shape of a hollow sphere (Kroto et al. (1985), Kroto (1988), Curl and Smalley (1988), Krätschmer et al. (1990)). Fullerenes are formed not only in hot and dense envelopes of evolved stars, but also identified in the tenuous and cold environment of interstellar clouds illuminated by strong ultraviolet radiation. The formation mechanism of this molecule in space is still unclear. The observed abundance of fullerene challenges the standard ion-molecule or grain-surface chemistry formation routes. Laboratory results showed an inhibition in the fullerene formation with the presence of hydrogen, while supporting the

formation of PAH (de Vries et al. (1993)). Another mechanism that is getting much interest in recent times is the top-down model whereby a photochemical processing of Hydrogenated amorphous carbon (HAC) grains results in the formation of PAH and fullerene (García-Hernández et al. (2010), Micelotta et al. (2012), Bernard-Salas et al. (2012)). The mid-IR vibrational modes of C_{60} lie at 18.9, 17.4, 8.5, 7.0 μm . The first astronomical detection of fullerene in the circumstellar environment of young PN, Tc1 was made by Cami et al. (2010). Fullerene was detected in young carbon-rich PNe in Milky Way galaxy (Bernard-Salas et al. (2012) & Otsuka et al. (2014)) and Magellanic clouds (Bernard-Salas et al. (2012)). Bernard-Salas et al. (2012) suggested that such physical conditions as found in these PNe could favour for the formation of fullerene. C_{60} had been detected in a few post-AGB binary stars earlier by Roberts et al. (2012) and Gielen et al. (2011) in a mixed oxygen-carbon rich environment. Zhang and Kwok (2011) had detected C_{60} in the PPN IRAS 01005+7910. All in all there are very few detections of C_{60} in late type stars. We carefully searched for C_{60} vibrational modes in the *Spitzer* IRS spectra of PAGB candidates in our sample. We detected vibrational modes of C_{60} for the first time in one of the PAGB candidate IRAS 21546+4721. To the best of our knowledge this is the first detection of C_{60} in this source and one of the very few detections reported yet. Figure 16 shows the vibrational modes of C_{60} observed in IRAS 21546+4721 compared with those of IRAS 01005+7910. The spectra of both the objects also show the C-C stretching and C-H bending modes of vibration of PAH. The vibrational transitions of fullerene at 17.4 and 18.9 μm are very clear in both the cases while those at 7.0 and 8.5 μm are blended with [Ar II] and PAH respectively. Modeling of the spectral energy distribution indicates a photospheric temperature greater than 10^4 K for both the sources. The presence of forbidden line of [NeII] in IRAS 21546+4721 further indicates its advanced stage of evolution. Also both the spectra show strong emissions of 30 μm feature (see Fig 16) that is attributed to MgS (Goebel and Moseley (1985)) or a carbonaceous compound (Zhang et al. (2009)). Otsuka et al. (2014) found the presence of 30 μm feature in all their sample Galactic PNe that have fullerene. Further, the absence of 21 μm feature in the mid-IR spectra of IRAS 21546+4721 and IRAS 01005+7910 rules out the possibility of fullerene as a carrier for this feature as suggested by Justtanont et al. (1996) & García-Lario et al. (1999).

8 CONCLUSIONS:

(i) Based on our analysis of *Spitzer* mid-infrared spectra of a fairly large sample of PAGB stars, we have broadly classified them into those having (a) strong/weak or blended PAH (b) silicate emission, in some cases along with PAH features (c) silicate absorption (d) prominent broad bump around $11\ \mu\text{m}$ and (e) nearly featureless spectra.

(ii) The SED modeling of the PAGB objects shows that the temperature of the inner dust shell decreases with increasing inner radius r_1 , while the ratio of r_1/r_c shows an increasing tendency with stellar photospheric temperature; the total mass loss rate correlates negatively with dust temperature and shows an increasing tendency with $\tau_{0.55}$.

(iii) The post-AGB mass loss rates obtained from the SED models are higher than those of the AGB and show correlation with the mass loss indices [K-12] and [25-2]. Dust mass loss rates obtained independently from the IR colors and *Spitzer* spectra also followed a similar trend.

(iv) The PAGB objects that show PAH emission features in the range $5\text{-}20\ \mu\text{m}$ indicate the onset of UV radiation from the central star and hence represent their advanced stage of evolution. The ratio of the observed strength of 7.7 and $11.2\ \mu\text{m}$ PAH feature showed an increasing trend with T_* , while decreasing with r_c . The peak wavelengths of the 6.2 , 7.7 and $11.2\ \mu\text{m}$ features seem to shift towards shorter wavelengths with increasing T_* .

(v) Nine objects in our sample showed fine structure line of Ne, indicating their transition nature from PAGB to PNe with the onset of ionisation.

(vi) Fullerene was detected for the first time in the PAGB star IRAS 21546+4721.

ACKNOWLEDGMENTS

This research was supported by the Department of Space, Government of India. The research has made use of the SIMBAD database operated at CDS, Strasbourg, France; the NASA/IPAC Infrared Science Archive, which is operated by the Jet Propulsion Laboratory, California Institute of Technology, under contract with the National Aeronautics and Space Administration, USA; and the data products from the Two Micron All Sky Survey, which is a joint project of the University of Massachusetts and the Infrared Processing and Analysis Center/California Institute of Technology, funded by the National Aeronautics and Space Administration and the National Science Foundation. We acknowledge the DUSTY

team for making available their codes for the astronomy community. We sincerely thank the anonymous referee for very useful comments which improved the quality of the paper.

REFERENCES

- B. G. Anandarao, S. R. Pottasch, and D. B. Vaidya. Circumstellar Dust in Mira Variables and the Mass Loss Mechanisms. *A&A*, 273:570, June 1993.
- R. A. Benjamin, E. Churchwell, B. L. Babler, T. M. Bania, D. P. Clemens, M. Cohen, J. M. Dickey, R. Indebetouw, J. M. Jackson, H. A. Kobulnicky, A. Lazarian, A. P. Marston, J. S. Mathis, M. R. Meade, S. Seager, S. R. Stolovy, C. Watson, B. A. Whitney, M. J. Wolff, and M. G. Wolfire. GLIMPSE. I. An SIRTf Legacy Project to Map the Inner Galaxy. *PASP*, 115:953–964, August 2003. doi:10.1086/376696.
- J. Bernard-Salas, E. Peeters, G. C. Sloan, S. Gutenkunst, M. Matsuura, A. G. G. M. Tielens, A. A. Zijlstra, and J. R. Houck. Unusual Dust Emission from Planetary Nebulae in the Magellanic Clouds. *ApJ*, 699:1541–1552, July 2009. doi:10.1088/0004-637X/699/2/1541.
- J. Bernard-Salas, J. Cami, E. Peeters, A. P. Jones, E. R. Micelotta, and M. A. T. Groenewegen. On the Excitation and Formation of Circumstellar Fullerenes. *ApJ*, 757:41, September 2012. doi:10.1088/0004-637X/757/1/41.
- A. Blasberger, E. Behar, H. B. Perets, N. Brosch, and A. G. G. M. Tielens. Observational Evidence Linking Interstellar UV Absorption to PAH Molecules. *ApJ*, 836:173, February 2017. doi:10.3847/1538-4357/aa5b8a.
- J. Bouwman, G. Meeus, A. de Koter, S. Hony, C. Dominik, and L. B. F. M. Waters. Processing of silicate dust grains in Herbig Ae/Be systems. *A&A*, 375:950–962, September 2001. doi:10.1051/0004-6361:20010878.
- V. Bujarrabal, A. Castro-Carrizo, J. Alcolea, and C. Sánchez Contreras. Mass, linear momentum and kinetic energy of bipolar flows in protoplanetary nebulae. *A&A*, 377:868–897, October 2001. doi:10.1051/0004-6361:20011090.
- J. Cami, J. Bernard-Salas, E. Peeters, and S. E. Malek. Detection of C₆₀ and C₇₀ in a Young Planetary Nebula. *Science*, 329:1180, September 2010. doi:10.1126/science.1192035.
- L. Cerrigone, J. L. Hora, G. Umana, and C. Triglilio. Spitzer Detection of Polycyclic Aromatic Hydrocarbons and Silicate Features in Post-AGB Stars and Young Planetary Nebulae. *ApJ*, 703:585–600, September 2009. doi:10.1088/0004-637X/703/1/585.
- A. Chalabaev and J. P. Maillard. On the rapid spectral variability of Be-stars: High spectral resolution study of Gamma Cas, Phi Per, and 59 CYG. *A&A*, 127:279–288, November 1983.
- A. N. Cox. *Allen’s astrophysical quantities*. 2000.
- R. F. Curl and R. E. Smalley. Probing C₆₀. *Science*, 242:1017–1022, November 1988. doi:10.1126/science.242.4881.1017.
- B. L. de Vries, J. A. D. L. Blommaert, L. B. F. M. Waters, C. Waelkens, M. Min, R. Lombaert, and H. Van Winckel. The problematically short superwind of OH/IR stars. Probing the outflow with the 69 μm spectral band of forsterite. *A&A*, 561:A75, January 2014. doi:10.1051/0004-6361/201322546.
- B. L. de Vries, K. M. Maaskant, M. Min, R. Lombaert, L. B. F. M. Waters, and J. A. D. L. Blommaert. Micron-sized forsterite grains in the pre-planetary nebula of IRAS 17150-3224. Searching for clues to the mysterious evolution of massive AGB stars. *A&A*, 576:A98, April 2015. doi:10.1051/0004-6361/201424843.
- M. S. de Vries, K. Reihls, H. R. Wendt, W. G. Golden, H. E. Hunziker, R. Fleming, E. Peterson, and S. Chang. A search for C₆₀ in carbonaceous chondrites. *Geochimica Cosmochimica Acta*, 57:933–938, February 1993. doi:10.1016/0016-7037(93)90179-Z.
- W. W. Duley. Chemical Evolution of Carbonaceous Material in Interstellar Clouds. *ApJ*, 528:841–848, January 2000. doi:10.1086/308204.
- M. P. Egan, S. D. Price, and K. E. Kraemer. The Midcourse Space Experiment Point Source Catalog Version 2.3. In *American Astronomical Society Meeting Abstracts*, volume 35 of *Bulletin of the American Astronomical Society*, page 1301, December 2003.

- F. Galliano, S. C. Madden, A. G. G. M. Tielens, E. Peeters, and A. P. Jones. Variations of the Mid-IR Aromatic Features inside and among Galaxies. *ApJ*, 679:310–345, May 2008. doi:10.1086/587051.
- D. A. García-Hernández, A. Manchado, P. García-Lario, L. Stanghellini, E. Villaver, R. A. Shaw, R. Szczerba, and J. V. Perea-Calderón. Formation of Fullerenes in H-containing Planetary Nebulae. *ApJ*, 724:L39–L43, November 2010. doi:10.1088/2041-8205/724/1/L39.
- P. García-Lario and J. V. Perea Calderón. The transition from AGB stars to planetary nebulae as seen by ISO. In C. Gry, S. Peschke, J. Matagne, P. Garcia-Lario, R. Lorente, and A. Salama, editors, *Exploiting the ISO Data Archive. Infrared Astronomy in the Internet Age*, volume 511 of *ESA Special Publication*, page 97, February 2003.
- P. García-Lario, A. Manchado, A. Ulla, and M. Manteiga. Infrared Space Observatory Observations of IRAS 16594-4656: A New Proto-Planetary Nebula with a Strong 21 Micron Dust Feature. *ApJ*, 513:941–946, March 1999. doi:10.1086/306895.
- C. Gielen, J. Cami, J. Bouwman, E. Peeters, and M. Min. Carbonaceous molecules in the oxygen-rich circumstellar environment of binary post-AGB stars. C₆₀ fullerenes and polycyclic aromatic hydrocarbons. *A&A*, 536:A54, December 2011. doi:10.1051/0004-6361/201117961.
- J. H. Goebel and S. H. Moseley. MgS grain component in circumstellar shells. *ApJ*, 290:L35–L39, March 1985. doi:10.1086/184437.
- L. Guzman-Ramirez, E. Lagadec, R. Wesson, A. A. Zijlstra, A. Müller, D. Jones, H. M. J. Boffin, G. C. Sloan, M. P. Redman, A. Smette, A. I. Karakas, and L.-Å. Nyman. Witnessing the emergence of a carbon star. *MNRAS*, 451:L1–L5, July 2015. doi:10.1093/mnras/slv055.
- G. Helou and D. W. Walker, editors. *Infrared astronomical satellite (IRAS) catalogs and atlases. Volume 7: The small scale structure catalog*, volume 7, 1988.
- S. Hony, C. Van Kerckhoven, E. Peeters, A. G. G. M. Tielens, D. M. Hudgins, and L. J. Allamandola. The CH out-of-plane bending modes of PAH molecules in astrophysical environments. *A&A*, 370:1030–1043, May 2001. doi:10.1051/0004-6361:20010242.
- S. N. Hoogzaad, F. J. Molster, C. Dominik, L. B. F. M. Waters, M. J. Barlow, and A. de Koter. The circumstellar dust shell of the post-AGB star HD 161796. *A&A*, 389:547–555, July 2002. doi:10.1051/0004-6361:20020403.
- J. R. Houck, T. L. Roellig, J. Van Cleve, W. J. Forrest, T. L. Herter, C. R. Lawrence, K. Matthews, H. J. Reitsema, B. T. Soifer, D. M. Watson, D. Weedman, M. Huisjen, J. R. Troeltzsch, D. J. Barry, J. Bernard-Salas, C. Blacken, B. R. Brandl, V. Charmandaris, D. Devost, G. E. Gull, P. Hall, C. P. Henderson, S. J. U. Higdon, B. E. Pirger, J. Schoenwald, G. C. Sloan, K. I. Uchida, P. N. Appleton, L. Armus, M. J. Burgdorf, S. B. Fajardo-Acosta, C. J. Grillmair, J. G. Ingalls, P. W. Morris, and H. I. Teplitz. The infrared spectrograph on the Spitzer Space Telescope. In J. C. Mather, editor, *Optical, Infrared, and Millimeter Space Telescopes*, volume 5487 of *Proc. SPIE*, pages 62–76, October 2004. doi:10.1117/12.550517.
- B. J. Hrivnak and J. H. Bieging. CO J = 2-1 and 4-3 Observations of Proto-planetary Nebulae: Time-variable Mass Loss. *ApJ*, 624:331–351, May 2005. doi:10.1086/428894.
- B. J. Hrivnak and S. Kwok. Discovery of Two New, Carbon-rich Proto-Planetary Nebulae: IRAS Z02229+6208 and IRAS 07430+1115. *ApJ*, 513:869–878, March 1999. doi:10.1086/306873.
- B. J. Hrivnak, K. Volk, and S. Kwok. 2-45 Micron Infrared Spectroscopy of Carbon-rich Proto-Planetary Nebulae. *ApJ*, 535: 275–292, May 2000. doi:10.1086/308823.
- B. J. Hrivnak, W. Lu, and K. A. Nault. Variability in Proto-planetary Nebulae. IV. Light Curve Analysis of Four Oxygen-rich, F Spectral Type Objects. *AJ*, 149:184, June 2015. doi:10.1088/0004-6256/149/6/184.
- D. Ishihara, T. Onaka, H. Kataza, A. Salama, C. Alfageme, A. Cassatella, N. Cox, P. García-Lario, C. Stephenson, M. Cohen, N. Fujishiro, H. Fujiwara, S. Hasegawa, Y. Ita, W. Kim, H. Matsuhara, H. Murakami, T. G. Müller, T. Nakagawa, Y. Ohyama, S. Oyabu, J. Pyo, I. Sakon, H. Shibai, S. Takita, T. Tanabé, K. Uemizu, M. Ueno, F. Usui, T. Wada, H. Watarai, I. Yamamura, and C. Yamauchi. The AKARI/IRC mid-infrared all-sky survey. *A&A*, 514:A1, May 2010. doi:10.1051/0004-6361/200913811.
- Z. Ivezic and M. Elitzur. Infrared emission and dynamics of outflows in late-type stars. *ApJ*, 445:415–432, May 1995.

[doi:10.1086/175707](https://doi.org/10.1086/175707).

- Z. Ivezić and M. Elitzur. Self-similarity and scaling behaviour of infrared emission from radiatively heated dust - I. Theory. *MNRAS*, 287:799–811, June 1997. [doi:10.1093/mnras/287.4.799](https://doi.org/10.1093/mnras/287.4.799).
- Z. Ivezić, M. Nenkova, and M. Elitzur. User Manual for DUSTY. *ArXiv Astrophysics e-prints*, October 1999.
- C. Jaeger, F. J. Molster, J. Dorschner, T. Henning, H. Mutschke, and L. B. F. M. Waters. Steps toward interstellar silicate mineralogy. IV. The crystalline revolution. *A&A*, 339:904–916, November 1998.
- K. Justtanont, M. J. Barlow, C. J. Skinner, P. F. Roche, D. K. Aitken, and C. H. Smith. Mid-infrared spectroscopy of carbon-rich post-AGB objects and detection of the PAH molecule chrysene. *A&A*, 309:612–628, May 1996.
- D. M. Kelly and B. J. Hrivnak. A 2 Micron H₂ Spectral Survey of Proto-Planetary Nebulae. *ApJ*, 629:1040–1054, August 2005. [doi:10.1086/431459](https://doi.org/10.1086/431459).
- W. Krätschmer, L. D. Lamb, K. Fostiropoulos, and D. R. Huffman. Solid C₆₀: a new form of carbon. *Nature*, 347:354–358, September 1990. [doi:10.1038/347354a0](https://doi.org/10.1038/347354a0).
- H. Kroto. Space, Stars, C₆₀, and Soot. *Science*, 242:1139–1145, November 1988. [doi:10.1126/science.242.4882.1139](https://doi.org/10.1126/science.242.4882.1139).
- H. W. Kroto, J. R. Heath, S. C. O'Brien, R. F. Curl, and R. E. Smalley. C(60): Buckminsterfullerene. *Nature*, 318:162, November 1985. [doi:10.1038/318162a0](https://doi.org/10.1038/318162a0).
- S. Kwok. The synthesis of organic and inorganic compounds in evolved stars. *Nature*, 430:985–991, August 2004. [doi:10.1038/nature02862](https://doi.org/10.1038/nature02862).
- S. Kwok. *The Origin and Evolution of Planetary Nebulae*. August 2007.
- S. Kwok and R. C. Bignell. Radio structure of the proto-planetary nebula GL 618. *ApJ*, 276:544–550, January 1984. [doi:10.1086/161643](https://doi.org/10.1086/161643).
- S. Kwok and P. A. Feldman. Discovery of radio brightening in AFGL 618. *ApJ*, 247:L67–L71, July 1981. [doi:10.1086/183591](https://doi.org/10.1086/183591).
- S. Kwok, K. Volk, and B. J. Hrivnak. Chemical evolution of carbonaceous materials in the last stages of stellar evolution. *A&A*, 350:L35–L38, October 1999.
- E. Lagadec, A. A. Zijlstra, M. Matsuura, J. W. Menzies, J. T. van Loon, and P. A. Whitelock. Dust mass-loss rates from asymptotic giant branch stars in the Fornax and Sagittarius dwarf spheroidal galaxies. *MNRAS*, 383:399–410, January 2008. [doi:10.1111/j.1365-2966.2007.12561.x](https://doi.org/10.1111/j.1365-2966.2007.12561.x).
- H. J. G. L. M. Lamers and J. P. Cassinelli. *Introduction to Stellar Winds*. June 1999.
- K. R. Lang. *Astrophysical formulae*. 1999.
- T. Le Bertre and J. M. Winters. On the relations between infrared colors and mass loss rates for Mira stars. *A&A*, 334:173–180, June 1998.
- V. Lebouteiller, B. Brandl, J. Bernard-Salas, D. Devost, and J. R. Houck. PAH Strength and the Interstellar Radiation Field around the Massive Young Cluster NGC 3603. *ApJ*, 665:390–401, August 2007. [doi:10.1086/519014](https://doi.org/10.1086/519014).
- A. Li and B. T. Draine. Infrared Emission from Interstellar Dust. II. The Diffuse Interstellar Medium. *ApJ*, 554:778–802, June 2001. [doi:10.1086/323147](https://doi.org/10.1086/323147).
- L. Likkell, T. Forveille, A. Omont, and M. Morris. CO observations of cold IRAS objects - AGB and post-AGB stars. *A&A*, 246:153–174, June 1991.
- J. S. Mathis, W. Rumpl, and K. H. Nordsieck. The size distribution of interstellar grains. *ApJ*, 217:425–433, October 1977. [doi:10.1086/155591](https://doi.org/10.1086/155591).
- M. Meixner, C. J. Skinner, J. R. Graham, E. Keto, J. G. Jernigan, and J. F. Arens. Axially Symmetric Superwinds of Proto-Planetary Nebulae with 21 Micron Dust Features. *ApJ*, 482:897–912, June 1997. [doi:10.1086/304174](https://doi.org/10.1086/304174).
- M. Meixner, T. Ueta, A. Dayal, J. L. Hora, G. Fazio, B. J. Hrivnak, C. J. Skinner, W. F. Hoffmann, and L. K. Deutsch. A Mid-infrared Imaging Survey of Proto-Planetary Nebula Candidates. *ApJS*, 122:221–242, May 1999. [doi:10.1086/313215](https://doi.org/10.1086/313215).
- E. R. Micelotta, A. P. Jones, J. Cami, E. Peeters, J. Bernard-Salas, and G. Fanchini. The Formation of Cosmic Fullerenes from Aromatic Clusters. *ApJ*, 761:35, December 2012. [doi:10.1088/0004-637X/761/1/35](https://doi.org/10.1088/0004-637X/761/1/35).
- A. Mishra, A. Li, and B. W. Jiang. On the Relation between the Mysterious 21 μm Emission Feature of Post-asymptotic Giant

- Branch Stars and Their Mass-loss Rates. *ApJ*, 825:68, July 2016. doi:10.3847/0004-637X/825/1/68.
- A. Omont, C. Loup, T. Forveille, P. te Lintel Hekkert, H. Habing, and P. Sivagnanam. Characterization and proportion of very cold C-rich circumstellar envelopes. *A&A*, 267:515–548, January 1993.
- M. Otsuka, F. Kemper, J. Cami, E. Peeters, and J. Bernard-Salas. Physical properties of fullerene-containing Galactic planetary nebulae. *MNRAS*, 437:2577–2593, January 2014. doi:10.1093/mnras/stt2070.
- E. Peeters, S. Hony, C. Van Kerckhoven, A. G. G. M. Tielens, L. J. Allamandola, D. M. Hudgins, and C. W. Bauschlicher. The rich 6 to 9 μm spectrum of interstellar PAHs. *A&A*, 390:1089–1113, August 2002. doi:10.1051/0004-6361:20020773.
- E. Peeters, C. W. Bauschlicher, Jr., L. J. Allamandola, A. G. G. M. Tielens, A. Ricca, and M. G. Wolfire. The PAH Emission Characteristics of the Reflection Nebula NGC 2023. *ApJ*, 836:198, February 2017. doi:10.3847/1538-4357/836/2/198.
- T. Posch, H. Mutschke, and A. Andersen. Reconsidering the Origin of the 21 Micron Feature: Oxides in Carbon-rich Protoplanetary Nebulae? *ApJ*, 616:1167–1180, December 2004. doi:10.1086/425113.
- K. R. G. Roberts, K. T. Smith, and P. J. Sarre. Detection of C_{60} in embedded young stellar objects, a Herbig Ae/Be star and an unusual post-asymptotic giant branch star. *MNRAS*, 421:3277–3285, April 2012. doi:10.1111/j.1365-2966.2012.20552.x.
- E. E. Salpeter. Formation and destruction of dust grains. *ARA&A*, 15:267–293, 1977. doi:10.1146/annurev.aa.15.090177.001411.
- D. Schoenberner. Late stages of stellar evolution. II - Mass loss and the transition of asymptotic giant branch stars into hot remnants. *ApJ*, 272:708–714, September 1983. doi:10.1086/161333.
- E. Sedlmayr and J. M. Winters. Grain Formation in the Winds of Cool Red Giant Stars. In R. F. Wing, editor, *The Carbon Star Phenomenon*, volume 177 of *IAU Symposium*, page 337, June 2000.
- M. F. Skrutskie, R. M. Cutri, R. Stiening, M. D. Weinberg, S. Schneider, J. M. Carpenter, C. Beichman, R. Capps, T. Chester, J. Elias, J. Huchra, J. Liebert, C. Lonsdale, D. G. Monet, S. Price, P. Seitzer, T. Jarrett, J. D. Kirkpatrick, J. E. Gizis, E. Howard, T. Evans, J. Fowler, L. Fullmer, R. Hurt, R. Light, E. L. Kopan, K. A. Marsh, H. L. McCallon, R. Tam, S. Van Dyk, and S. Wheelock. The Two Micron All Sky Survey (2MASS). *AJ*, 131:1163–1183, February 2006. doi:10.1086/498708.
- G. C. Sloan, K. E. Kraemer, S. D. Price, and R. F. Shipman. A Uniform Database of 2.4–45.4 Micron Spectra from the Infrared Space Observatory Short Wavelength Spectrometer. *ApJS*, 147:379–401, August 2003. doi:10.1086/375443.
- G. C. Sloan, L. D. Keller, W. J. Forrest, E. Leibensperger, B. Sargent, A. Li, J. Najita, D. M. Watson, B. R. Brandl, C. H. Chen, J. D. Green, F. Markwick-Kemper, T. L. Herter, P. D’Alessio, P. W. Morris, D. J. Barry, P. Hall, P. C. Myers, and J. R. Houck. Mid-Infrared Spectra of Polycyclic Aromatic Hydrocarbon Emission in Herbig Ae/Be stars. *ApJ*, 632:956–963, October 2005. doi:10.1086/444371.
- G. C. Sloan, M. Jura, W. W. Duley, K. E. Kraemer, J. Bernard-Salas, W. J. Forrest, B. Sargent, A. Li, D. J. Barry, C. J. Bohac, D. M. Watson, and J. R. Houck. The Unusual Hydrocarbon Emission from the Early Carbon Star HD 100764: The Connection between Aromatics and Aliphatics. *ApJ*, 664:1144–1153, August 2007. doi:10.1086/519236.
- J. D. T. Smith, B. T. Draine, D. A. Dale, J. Moustakas, R. C. Kennicutt, Jr., G. Helou, L. Armus, H. Roussel, K. Sheth, G. J. Bendo, B. A. Buckalew, D. Calzetti, C. W. Engelbracht, K. D. Gordon, D. J. Hollenbach, A. Li, S. Malhotra, E. J. Murphy, and F. Walter. The Mid-Infrared Spectrum of Star-forming Galaxies: Global Properties of Polycyclic Aromatic Hydrocarbon Emission. *ApJ*, 656:770–791, February 2007. doi:10.1086/510549.
- A. K. Speck and A. M. Hofmeister. Processing of Presolar Grains around Post-Asymptotic Giant Branch Stars: Silicon Carbide as the Carrier of the 21 Micron Feature. *ApJ*, 600:986–991, January 2004. doi:10.1086/379973.
- A. K. Speck, G. D. Thompson, and A. M. Hofmeister. The Effect of Stellar Evolution on SiC Dust Grain Sizes. *ApJ*, 634:426–435, November 2005. doi:10.1086/496955.
- H. W. W. Spoon, J. A. Marshall, J. R. Houck, M. Elitzur, L. Hao, L. Armus, B. R. Brandl, and V. Charmandaris. Mid-Infrared Galaxy Classification Based on Silicate Obscuration and PAH Equivalent Width. *ApJ*, 654:L49–L52, January 2007. doi:10.1086/511268.
- O. Suárez, P. García-Lario, A. Manchado, M. Manteiga, A. Ulla, and S. R. Pottasch. A spectroscopic atlas of post-AGB stars and planetary nebulae selected from the IRAS point source catalogue. *A&A*, 458:173–180, October 2006. doi:10.1051/0004-6361:20054108.

- R. Szczerba, N. Siódmiak, G. Stasińska, and J. Borkowski. An evolutionary catalogue of galactic post-AGB and related objects. *A&A*, 469:799–806, July 2007. doi:10.1051/0004-6361:20067035.
- A. G. G. M. Tielens. *The Physics and Chemistry of the Interstellar Medium*. August 2005.
- K. I. Uchida, K. Sellgren, M. W. Werner, and M. L. Houdashelt. Infrared Space Observatory Mid-Infrared Spectra of Reflection Nebulae. *ApJ*, 530:817–833, February 2000. doi:10.1086/308379.
- T. Ueta, M. Meixner, and M. Bobrowsky. A Hubble Space Telescope Snapshot Survey of Proto-Planetary Nebula Candidates: Two Types of Axisymmetric Reflection Nebulosity. *ApJ*, 528:861–884, January 2000. doi:10.1086/308208.
- T. Ueta, M. Meixner, P. M. Hinz, W. F. Hoffmann, W. Brandner, A. Dayal, L. K. Deutsch, G. G. Fazio, and J. L. Hora. Subarcsecond Mid-Infrared Structure of the Dust Shell around IRAS 22272+5435. *ApJ*, 557:831–843, August 2001. doi:10.1086/322259.
- W. E. C. J. van der Veen and H. J. Habing. The IRAS two-colour diagram as a tool for studying late stages of stellar evolution. *A&A*, 194:125–134, April 1988.
- H. van Winckel. Post-AGB Stars. *ARA&A*, 41:391–427, 2003. doi:10.1146/annurev.astro.41.071601.170018.
- E. Vassiliadis and P. R. Wood. Post-asymptotic giant branch evolution of low- to intermediate-mass stars. *ApJS*, 92:125–144, May 1994. doi:10.1086/191962.
- V. Venkata Raman and B. G. Anandarao. Infrared spectroscopic study of a selection of AGB and post-AGB stars. *MNRAS*, 385:1076–1086, April 2008. doi:10.1111/j.1365-2966.2008.12915.x.
- G. von Helden, A. G. G. M. Tielens, D. van Heijnsbergen, M. A. Duncan, S. Hony, L. B. F. M. Waters, and G. Meijer. Titanium Carbide Nanocrystals in Circumstellar Environments. *Science*, 288:313–316, April 2000. doi:10.1126/science.288.5464.313.
- C. Waelkens and R. B. F. M. Waters. Post-AGB Stars. In H. J. Habing and H. Olofsson, editors, *Asymptotic giant branch stars, by Harm J. Habing and Hans Olofsson. Astronomy and astrophysics library, New York, Berlin: Springer, 2003, 2003.*
- L. B. F. M. Waters, J. Cami, T. de Jong, F. J. Molster, J. T. van Loon, J. Bouwman, A. de Koter, C. Waelkens, H. Van Winckel, P. W. Morris, J. Cami, J. Bouwman, A. de Koter, T. de Jong, and T. de Graauw. An oxygen-rich dust disk surrounding an evolved star in the Red Rectangle. *Nature*, 391:868, February 1998. doi:10.1038/36052.
- P. Woitke, A. Goeres, and E. Sedlmayr. On the gas temperature in the shocked circumstellar envelopes of pulsating stars. II. Shock induced condensation around R Coronae Borealis stars. *A&A*, 313:217–228, September 1996.
- A. W. Woodsworth, S. Kwok, and S. J. Chan. CO observations of proto-planetary nebulae exhibiting the unidentified feature at 21 microns. *A&A*, 228:503–505, February 1990.
- K. Zhang, B. W. Jiang, and A. Li. On Magnesium Sulfide as the Carrier of the 30 μm Emission Feature in Evolved Stars. *ApJ*, 702:680–685, September 2009. doi:10.1088/0004-637X/702/1/680.
- Y. Zhang and S. Kwok. Detection of C₆₀ in the Protoplanetary Nebula IRAS 01005+7910. *ApJ*, 730:126, April 2011. doi:10.1088/0004-637X/730/2/126.
- Y. Zhang, S. Kwok, and B. J. Hrivnak. A Spitzer/Infrared Spectrograph Spectral Study of a Sample of Galactic Carbon-rich Proto-planetary Nebulae. *ApJ*, 725:990–1001, December 2010. doi:10.1088/0004-637X/725/1/990.

Table 1: Source of spectra and dust classification of the PAGB objects

Object name	Source of spectra	Dust classification
01005+7910	<i>Spitzer</i> SL, LL, SH	PAH
04296+3429	<i>Spitzer</i> SL, SH, LH	PAH
05089+0459	<i>Spitzer</i> SH	Not classified
05113+1347	<i>Spitzer</i> SH	PAH
05341+0852	<i>Spitzer</i> SH, LH	PAH
06034+1354	<i>Spitzer</i> SH, LH	Sil emission
06530-0213	<i>Spitzer</i> SH, LH	PAH
06556+1623	<i>Spitzer</i> SL, LL	Not classified
07134+1005	<i>Spitzer</i> SH, ISO	PAH
08005-2356	<i>Spitzer</i> SH, LH	11 micron source
08335-4026	<i>Spitzer</i> SL, LL	PAH+Sil
10211-5922	<i>Spitzer</i> SL, SH, LH	Sil emission
11201-6545	<i>Spitzer</i> SL, SH, LH	Sil emission
11339-6004	<i>Spitzer</i> SL, SH, LH	11 micron source
11353-6037	<i>Spitzer</i> SL, SH, LH	PAH+Sil
11387-6113	<i>Spitzer</i> SL, SH, LH	PAH+Sil
12145-5834	<i>Spitzer</i> SL, LL	PAH
13245-5036	<i>Spitzer</i> SL, LL	Not classified
13313-5838	<i>Spitzer</i> SL, LL	PAH
13500-6106	<i>Spitzer</i> SL, SH, LH	Sil absorption
13529-5934	<i>Spitzer</i> SL, SH, LH	Not classified
14325-6428	<i>Spitzer</i> SL, SH, LH	11 micron source
14341-6211	<i>Spitzer</i> SL, SH, LH	11 micron source
14346-5952	<i>Spitzer</i> SH, LH	Not classified
14429-4539	<i>Spitzer</i> SL, SH, LH	PAH
14482-5725	<i>Spitzer</i> SL, LL	PAH+Sil
15482-5741	<i>Spitzer</i> SL, LL	PAH
16206-5956	<i>Spitzer</i> SL, SH, LH	Sil emission
16494-3930	<i>Spitzer</i> SH, LH	11 micron source
16559-2957	<i>Spitzer</i> SL, SH, LH	Not classified
17009-4154	<i>Spitzer</i> SH	PAH
17074-1845	<i>Spitzer</i> SL, LL	Sil emission
17088-4221	<i>Spitzer</i> SH	Not classified
17130-4029	<i>Spitzer</i> SL, SH, LH	PAH
17168-3736	<i>Spitzer</i> SH, LH	Sil absorption
17195-2710	<i>Spitzer</i> SL, SH, LH	Sil absorption
17203-1534	<i>Spitzer</i> SL, LL	Sil emission
17234-4008	<i>Spitzer</i> SL, SH, LH	Sil absorption
17253-2831	<i>Spitzer</i> SL, LL, SH, LH	Sil absorption
17287-3443	<i>Spitzer</i> SL, SH	Transition object with peculiar dust
17311-4924	<i>Spitzer</i> SL, LL	Transition object with peculiar dust

Continued on next page

Table 1 – *continued from previous page*

Object name	Source of spectra	Dust classification
17317-2743	<i>Spitzer</i> SL, SH, LH	Sil emission
17359-2902	<i>Spitzer</i> SL, SH, LH	11 micron source
17364-1238	<i>Spitzer</i> SL, LL	Sil emission
17376-2040	<i>Spitzer</i> SL, LL	Not classified
17381-1616	<i>Spitzer</i> SL, LL	Sil emission
17423-1755	<i>Spitzer</i> SL, LL, <i>ISO</i>	featureless
17488-1741	<i>Spitzer</i> SL, LL	Not classified
17542-0603	<i>Spitzer</i> SL, LL	PAH+Sil
17580-3111	<i>Spitzer</i> SL, SH, LH	Not classified
18023-3409	<i>Spitzer</i> SL, LL	Sil emission
18062+2410	<i>Spitzer</i> SL, LL	Sil emission
18246-1032	<i>Spitzer</i> SL, SH, LH	Sil absorption
18533+0523	<i>Spitzer</i> SL, SH, LH	PAH
19024+0044	<i>Spitzer</i> SL, SH, LH	PAH + sil
19157-0247	<i>Spitzer</i> SL, LL, SH, LH	Sil emission
19200+3457	<i>Spitzer</i> SL, LL	PAH
19306+1407	<i>Spitzer</i> SL, LL, SH	PAH+Sil
19454+2920	<i>Spitzer</i> SH	featureless
19477+2401	<i>Spitzer</i> SH, LH	Not classified
19590-1249	<i>Spitzer</i> SL, LL	Sil emission
20259+4206	<i>Spitzer</i> SH, LH	featureless
20462+3416	<i>Spitzer</i> SL, LL	PAH+Sil
20572+4919	<i>Spitzer</i> SL, LL	Sil emission
21289+5815	<i>Spitzer</i> SL, LL	PAH+Sil
21546+4721	<i>Spitzer</i> SL, LL	PAH
22023+5249	<i>Spitzer</i> SL, LL	PAH+Sil
22036+5306	<i>Spitzer</i> SH, LH	Sil absorption
22223+4327	<i>Spitzer</i> SL, LL, SH, LH	PAH
F22327-1731	<i>Spitzer</i> SL, SH, LH	Sil emission
23304+6147	<i>Spitzer</i> SH, LH, <i>ISO</i>	PAH

Table 2. Equivalent widths (in μm) and peak wavelengths (in μm) of PAH features in the sample PAGB candidates

Name	Equivalent width			Peak wavelength		
	6.2 μm	7.7 μm	11.2 μm	6.2 μm	7.7 μm	11.2 μm
01005+7910	0.380±0.034	0.379±0.020	0.058±0.005	6.225±0.003	7.555±0.006	11.241±0.003
04296+3429	0.158±0.007	0.183±0.025	0.092±0.008	6.262±0.002	7.829±0.068	11.369±0.013
05113+1347	-	-	0.040±0.005	-	-	11.355±0.004
05341+0852	-	-	0.082±0.006	-	-	11.352±0.003
06530-0213	-	-	0.132±0.027	-	-	11.357±0.007
07134+1005	-	-	0.194±0.017	-	-	11.346±0.004
08335-4026	0.078±0.006	0.108±0.020	0.031±0.006	6.239±0.003	7.703±0.030	11.243±0.002
11353-6037	0.503±0.019	0.514±0.028	0.074±0.005	6.252±0.009	7.773±0.004	11.258±0.003
11387-6113	0.056±0.006	0.050±0.005	-	6.307±0.003	7.893±0.021	-
12145-5834	0.438±0.016	0.368±0.029	0.112±0.009	6.235±0.002	7.597±0.006	11.255±0.007
13313-5838	0.019±0.006	-	-	6.285±0.006	-	-
14429-4539	0.216±0.030	0.356±0.023	0.100±0.019	6.267±0.006	7.938±0.007	11.311±0.006
14482-5725	0.041±0.008	0.105±0.020	0.048±0.006	6.298±0.003	8.164±0.012	11.238±0.011
15482-5741	0.114±0.025	0.266±0.022	0.048±0.005	6.262±0.010	7.968±0.009	11.297±0.009
17009-4154	-	-	0.049±0.006	-	-	11.253±0.003
17130-4029	0.051±0.007	0.174±0.014	-	6.275±0.009	8.065±0.013	-
17542-0603	0.011±0.007	0.013±0.005	0.057±0.006	6.312±0.002	7.899±0.002	11.305±0.011
18533+0523	0.072±0.009	0.562±0.007	0.011±0.004	6.282±0.002	7.991±0.004	11.260±0.011
19024+0044	0.090±0.004	0.021±0.004	-	6.265±0.002	7.740±0.006	-
19200+3457	0.441±0.009	0.241±0.041	0.212±0.040	6.232±0.002	7.590±0.014	11.268±0.004
19306+1407	0.339±0.005	0.251±0.021	0.006±0.003	6.239±0.007	7.820±0.008	11.242±0.011
20462+3416	0.215±0.025	0.343±0.007	0.012±0.064	6.233±0.007	7.692±0.018	11.254±0.018
21289+5815	0.100±0.029	0.069±0.005	0.016±0.005	6.241±0.007	7.832±0.017	11.238±0.014
21546+4721	0.170±0.009	0.117±0.034	0.007±0.002	6.226±0.002	7.592±0.014	11.226±0.002
22023+5249	0.304±0.038	0.373±0.058	0.025±0.005	6.220±0.002	7.743±0.009	11.218±0.006
22223+4327	0.025±0.004	0.099±0.009	0.032±0.006	6.267±0.004	7.880±0.028	11.287±0.004
23304+6147	-	-	0.089±0.004	-	-	11.360±0.008

Table 3. Parameters derived from SED modeling of PAGB candidates using DUSTY; the spectral types are from SIMBAD and [Suárez et al. \(2006\)](#) and both the total and dust mass-loss rates are in the unit of $M_{\odot}\text{yr}^{-1}$

Object	Sp.Type	T_*	T_d	$\tau_{0.55}$	Grain type	r_1 (m)	r_1/r_c	\dot{M}	\dot{M}_d
05089+0459	M3I	3500	200	6.0	AmC(1.0)	2.1E+14	1.1E+03	5.8E-05	4.4E-09
06034+1354	–	5000	300	1.5	AmC(0.9)+Sil(0.1)	7.6E+13	8.2E+02	1.9E-05	2.2E-09
06556+1623	Bpe	15000	240	0.3	AmC(0.6)+Gr(0.4)	2.1E+14	2.1E+04	1.5E-05	6.1E-10
08005-2356	F5e	6650	440	5.0	Gr(0.9)+SiC(0.1)	5.4E+13	1.0E+03	3.1E-05	8.1E-10
10211-5922	–	5000	250	0.3	Gr(0.9)+Sil(0.1)	1.1E+14	1.2E+03	7.5E-06	1.4E-10
11201-6545	A3Ie	6000	150	5.0	Sil(0.5)+AmC(0.5)	3.5E+14	5.5E+03	8.7E-05	2.0E-09
11339-6004	–	14000	190	8.0	AmC(0.9)+SiC(0.1)	4.0E+14	3.4E+04	1.0E-04	7.6E-08
13245-5036	A7Ie	7650	200	7.0	AmC(1.0)	2.9E+14	7.5E+04	8.2E-05	1.5E-10
13500-6106	–	11000	280	20.0	AmC(0.1)+Gr(0.1)+Sil(0.8)	8.2E+13	4.2E+03	1.0E-04	2.9E-08
13529-5934	–	12000	200	13.0	AmC(0.2)+Gr(0.8)	3.6E+14	2.2E+04	1.2E-04	1.8E-08
14325-6428	F5I	6640	160	2.5	AmC(0.9)+SiC(0.1)	5.0E+14	9.6E+03	6.6E-05	1.6E-09
14341-6211	–	6000	195	10.0	AmC(0.9)+SiC(0.1)	2.9E+14	4.5E+03	9.5E-05	1.9E-08
14346-5952	–	12000	500	10.0	Gr(0.9)+AmC(0.1)	5.0E+13	3.1E+03	4.0E-05	5.5E-10
16206-5956	A3Iab:e	8000	105	0.7	AmC(0.3)+Sil(0.7)	7.6E+14	2.1E+04	5.1E-05	1.9E-10
16494-3930	G2I	5160	200	8.0	AmC(0.8)+Gr(0.1)+SiC(0.1)	2.5E+14	2.9E+03	7.9E-05	8.2E-08
16559-2957	F5Iab:e	6650	220	4.0	AmC(0.7)+Sil(0.3)	1.6E+14	3.1E+03	5.1E-05	1.0E-08
17074-1845	B5Ibe	11000	140	3.0	Sil(1.0)	3.3E+14	1.7E+04	1.0E-04	2.1E-09
17088-4221	–	14000	250	15.0	AmC(0.1)+Gr(0.9)	2.4E+14	2.1E+04	1.0E-04	6.1E-08
17168-3736	–	14000	190	12.0	Gr(0.9)+Sil(0.1)	3.9E+14	3.3E+04	1.2E-04	9.4E-08
17195-2710	–	8000	370	9.0	Gr(0.9)+Sil(0.1)	8.1E+13	2.2E+03	5.0E-05	2.6E-09
17203-1534	B1IIIpe	10000	130	2.5	Gr(0.3)+Sil(0.7)	5.0E+14	2.1E+04	9.0E-05	1.4E-09
17234-4008	–	14000	175	10.0	Gr(0.9)+Sil(0.1)	4.6E+14	3.9E+04	1.2E-04	1.7E-08
17253-2831	–	5000	150	4.0	AmC(0.7)+Gr(0.2)+Sil(0.1)	4.5E+14	4.9E+03	7.6E-05	1.3E-09
17287-3443	–	18000	150	20.0	AmC(0.3)+Gr(0.7)	7.4E+14	1.0E+05	2.0E-04	1.9E-08
17311-4924	B1Iae	15000	200	3.0	Gr(0.4)+Sil(0.6)	2.3E+14	2.9E+04	6.7E-05	2.4E-10
17317-2743	F5I	6640	140	7.5	Gr(0.9)+Sil(0.1)	5.2E+14	9.9E+03	1.1E-04	4.1E-10
17359-2902	–	8000	230	15.0	Gr(0.9)+SiC(0.1)	2.4E+14	6.6E+03	1.0E-04	5.3E-09
17364-1238	–	8000	130	1.0	AmC(0.1)+Sil(0.9)	3.2E+14	8.9E+03	4.6E-05	3.4E-10
17376-2040	F6I	6460	280	4.0	AmC(0.5)+Gr(0.5)	1.2E+14	2.2E+03	4.1E-05	9.1E-10
17381-1616	B1Ibe	20700	400	1.0	AmC(0.9)+Sil(0.1)	5.7E+13	1.0E+04	1.7E-05	5.1E-09
17423-1755	Be	13000	170	5.0	Gr(0.8)+Sil(0.2)	4.0E+14	2.6E+04	8.6E-05	7.7E-10
17488-1741	F7I	6280	260	6.5	Gr(1.0)	1.6E+14	2.8E+03	6.0E-05	1.6E-10
17580-3111	–	5000	290	15.0	Gr(1.0)	1.1E+14	1.2E+03	7.3E-05	1.2E-08
18023-3409	B2IIIe	10000	175	1.0	AmC(0.3)+Sil(0.7)	2.2E+14	9.6E+03	3.7E-05	3.0E-09
18062+2410	B1IIIpe	18000	200	1.0	Sil(1.0)	1.9E+14	2.6E+04	4.5E-05	4.0E-08
18246-1032	–	20000	130	20.0	Gr(0.8)+Sil(0.2)	8.5E+14	1.3E+05	2.2E-04	2.6E-08
19157-0247	B1III	15000	800	2.0	Gr(0.8)+Sil(0.2)	1.5E+13	1.5E+03	1.2E-05	1.5E-09
19454+2920	–	10000	180	7.0	AmC(1.0)	4.2E+14	1.8E+04	9.7E-05	4.1E-08
19477+2401	F4I	6820	200	10.0	AmC(0.8)+Gr(0.2)	2.8E+14	5.7E+03	9.7E-05	2.7E-10
19590-1249	B1Ibe	20000	125	0.1	Gr(0.3)+Sil(0.7)	7.1E+14	1.2E+05	1.8E-05	1.0E-09
20259+4206	F3I	6990	200	8.0	AmC(1.0)	2.9E+14	6.1E+03	8.5E-05	2.3E-08
20572+4919	F3Ie	7700	265	2.0	Gr(0.85)+Sil(0.15)	1.2E+14	2.9E+03	2.9E-05	8.3E-10
22036+5306	–	8000	140	8.0	AmC(0.7)+Gr(0.2)+Sil(0.1)	6.7E+14	1.8E+04	1.3E-04	1.3E-09
F22327-1731	A0III	7600	600	0.35	Gr(0.85)+Sil(0.15)	2.2E+13	5.5E+02	4.6E-06	7.5E-10

Table 4. Parameters derived with two shells in the SED modeling using DUSTY for the PAGB candidates; the spectral types are from SIMBAD and both the total mass-loss rates are in the unit of $M_{\odot}\text{yr}^{-1}$

Objects	Sp. Type	T_*	Sphere1			Sphere2			\dot{M}		
			PAH type	T_d	r_1 (m)	r_1/r_c	Grain type	T_d		r_1 (m)	r_1/r_c
01005+7910	B2Iab:e	15000	ionised	700	3.1E+13	3.0E+03	Gr(1.0)	250	2.5E+14	2.4E+04	4.0E-05
04296+3429	G0Ia	5510	ionised	600	1.9E+13	2.5E+02	AmC(0.9)+Gr(0.1)	200	2.6E+14	3.4E+03	6.6E-05
05113+1347	G8Ia	4900	neutral	250	1.5E+14	1.6E+03	AmC(1.0)	200	2.4E+14	2.5E+03	4.7E-05
05341+0852	F4Iab	6820	neutral	500	4.2E+13	8.4E+02	Gr(1.0)	350	9.6E+13	1.9E+03	3.4E-05
06530-0213	F0Iab:	7300	neutral	250	2.4E+14	5.6E+02	Gr(1.0)	100	1.2E+15	2.8E+04	5.0E-05
07134+1005	F5Iab:	6650	neutral	600	2.5E+13	4.7E+02	AmC(1.0)	150	6.1E+14	1.1E+04	3.4E-05
08335-4026	B8e	11500	ionised	700	2.7E+13	1.5E+03	Gr(0.95)+Sil(0.05)	100	1.3E+15	7.9E+04	1.2E-05
11353-6037	B5Ie	13400	ionised	500	7.3E+13	5.6E+03	Gr(1.0)	220	3.0E+14	2.3E+04	6.4E-05
11387-6113	A3I	8890	neutral	190	5.4E+14	1.85E+04	Gr(0.8)+Sil(0.2)	150	4.7E+14	1.6E+04	7.2E-05
12145-5834	-	10000	ionised	500	5.9E+13	2.5E+03	Gr(1.0)	100	1.3E+15	5.7E+04	7.4E-05
13313-5838	KIII	4600	neutral	400	4.8E+13	4.4E+02	Gr(0.2)+AmC(0.8)	200	2.3E+14	2.1E+03	3.1E-05
14429-4539	F4I	6820	ionised	400	7.0E+13	1.4E+03	Gr(0.6)+AmC(0.4)	320	9.7E+13	1.9E+03	4.1E-05
14482-5725	A2I	9080	neutral	400	4.2E+13	2.9E+02	Gr(1.0)	300	9.1E+13	6.2E+02	3.6E-05
15482-5741	F7I	6100	ionised	400	6.1E+13	9.9E+02	AmC(1.0)	150	5.9E+14	9.4E+03	8.3E-05
17009-4154	-	4500	neutral	250	1.4E+14	1.2E+03	Gr(1.0)	100	8.9E+14	7.8E+03	8.7E-05
17130-4029	-	14000	ionised	1300	5.7E+12	4.8E+02	Gr(0.2)+AmC(0.8)	120	1.2E+15	1.0E+05	6.5E-05
17542-0603	Ge	5500	ionised	1000	5.0E+12	6.5E+01	Gr(1.0)	500	3.7E+13	4.8E+02	1.6E-05
18533+0523	-	5000	ionised	400	5.0E+13	5.4E+02	Gr(0.7)+AmC(0.3)	100	1.0E+15	1.1E+04	9.4E-05
19024+0044	-	10000	ionised	1200	5.6E+12	2.4E+02	AmC(0.8)+Sil(0.2)	130	8.4E+14	3.6E+04	1.1E-04
19200+3457	B...	12000	ionised	500	6.7E+13	4.1E+03	Gr(1.0)	230	2.5E+14	1.5E+04	1.5E-05
19306+1407	B0:e	15400	ionised	800	2.2E+13	2.3E+03	Gr(1.0)	100	1.6E+15	1.6E+05	8.9E-05
20462+3416	B1Iae	20800	ionised	150	1.5E+15	2.9E+05	Gr(0.5)+AmC(0.5)	100	1.7E+15	3.3E+05	1.7E-05
21289+5815	A2Ie	7000	ionised	700	1.7E+13	3.5E+02	Gr(0.7)+Sil(0.3)	300	8.6E+13	1.8E+03	3.9E-05
21546+4721	-	10000	ionised	500	5.9E+13	2.5E+03	Gr(1.0)	200	3.4E+14	1.4E+04	4.3E-05
22023+5249	Be	12000	ionised	200	6.1E+14	3.8E+04	Gr(0.2)+AmC(0.8)	160	5.9E+14	3.6E+04	8.7E-05
22223+4327	F9Ia	6100	ionised	700	1.4E+13	2.3E+02	Gr(1.0)	180	3.2E+14	5.2E+03	3.7E-05
23304+6147	G2Ia	5200	neutral	400	5.5E+13	6.4E+02	Gr(0.5)+AmC(0.5)	170	3.6E+14	4.1E+03	4.3E-05

APPENDIX A: CONTINUUM-SUBTRACTED SPITZER IRS SPECTRA OF THE SAMPLE PAGB STARS

The Continuum-subtracted *Spitzer* IRS spectra in the wavelength region 5 - 38 μm are shown in the following figures, arranged in the category-wise (see text for details).

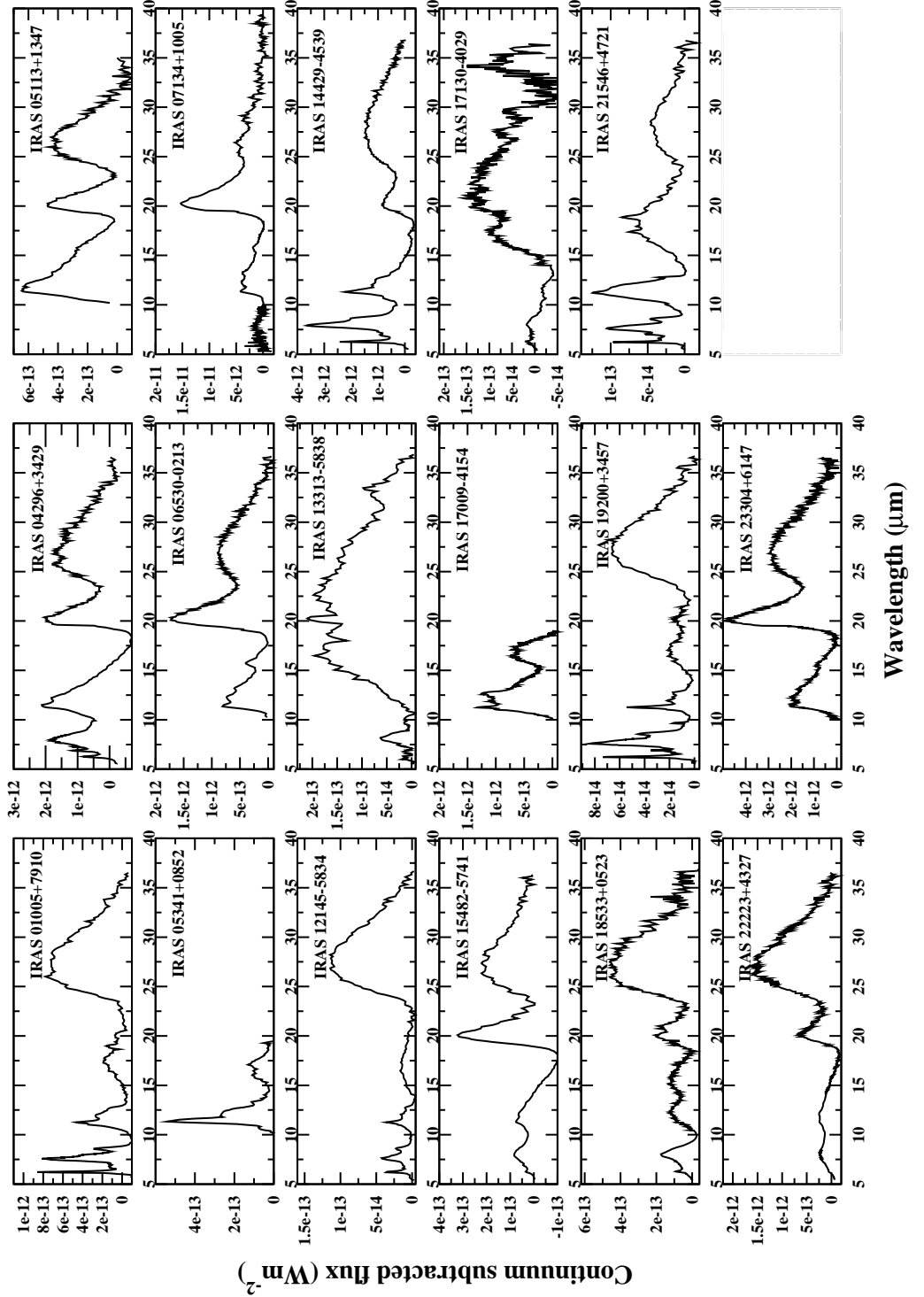


Figure A1. Continuum-subtracted *Spitzer* IRS spectra for sources with PAH emissions (Classes 1a, 1b, 1c)

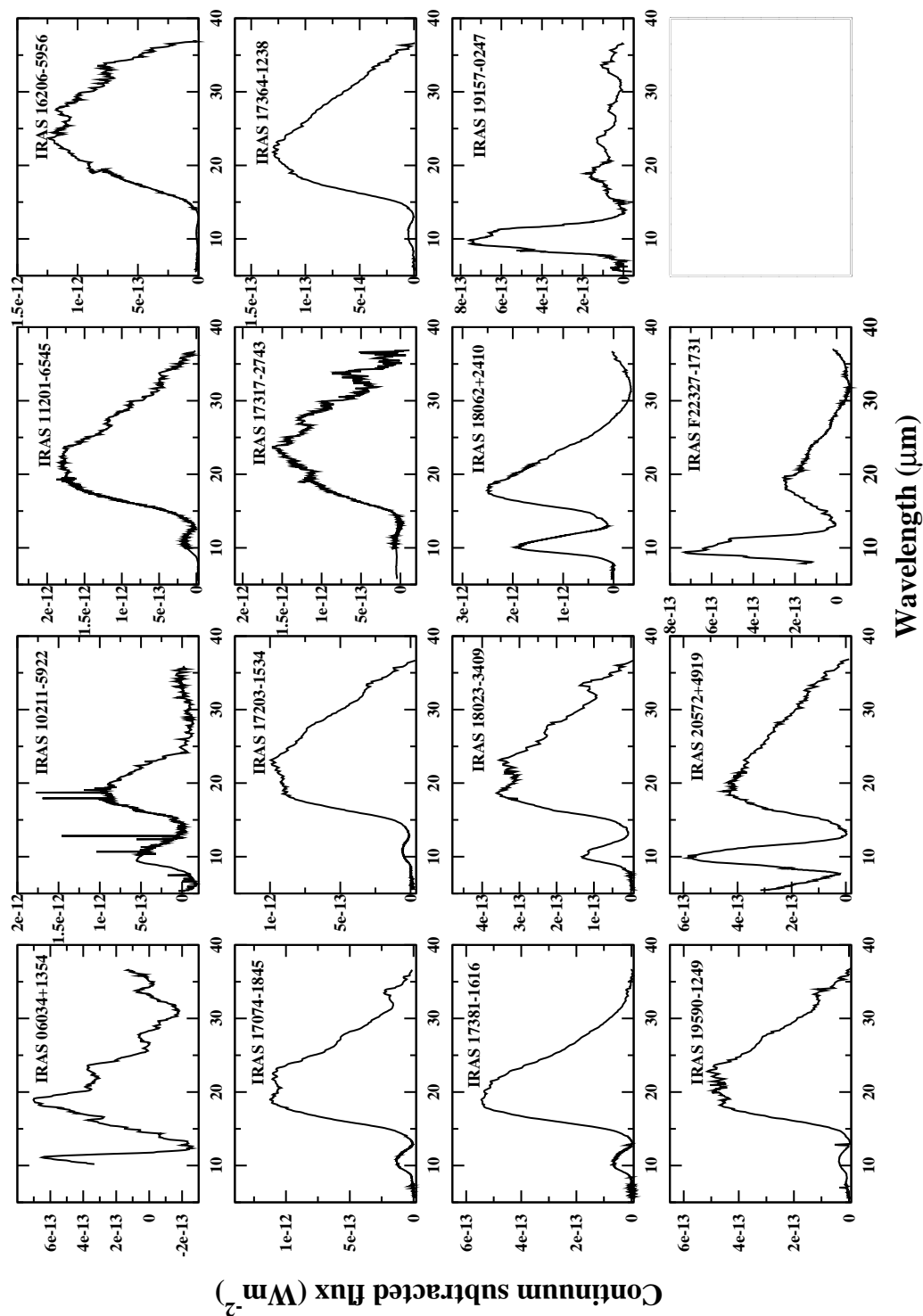


Figure A2. Continuum-subtracted *Spitzer* IRS spectra for sources with silicate emission (Class 2a)

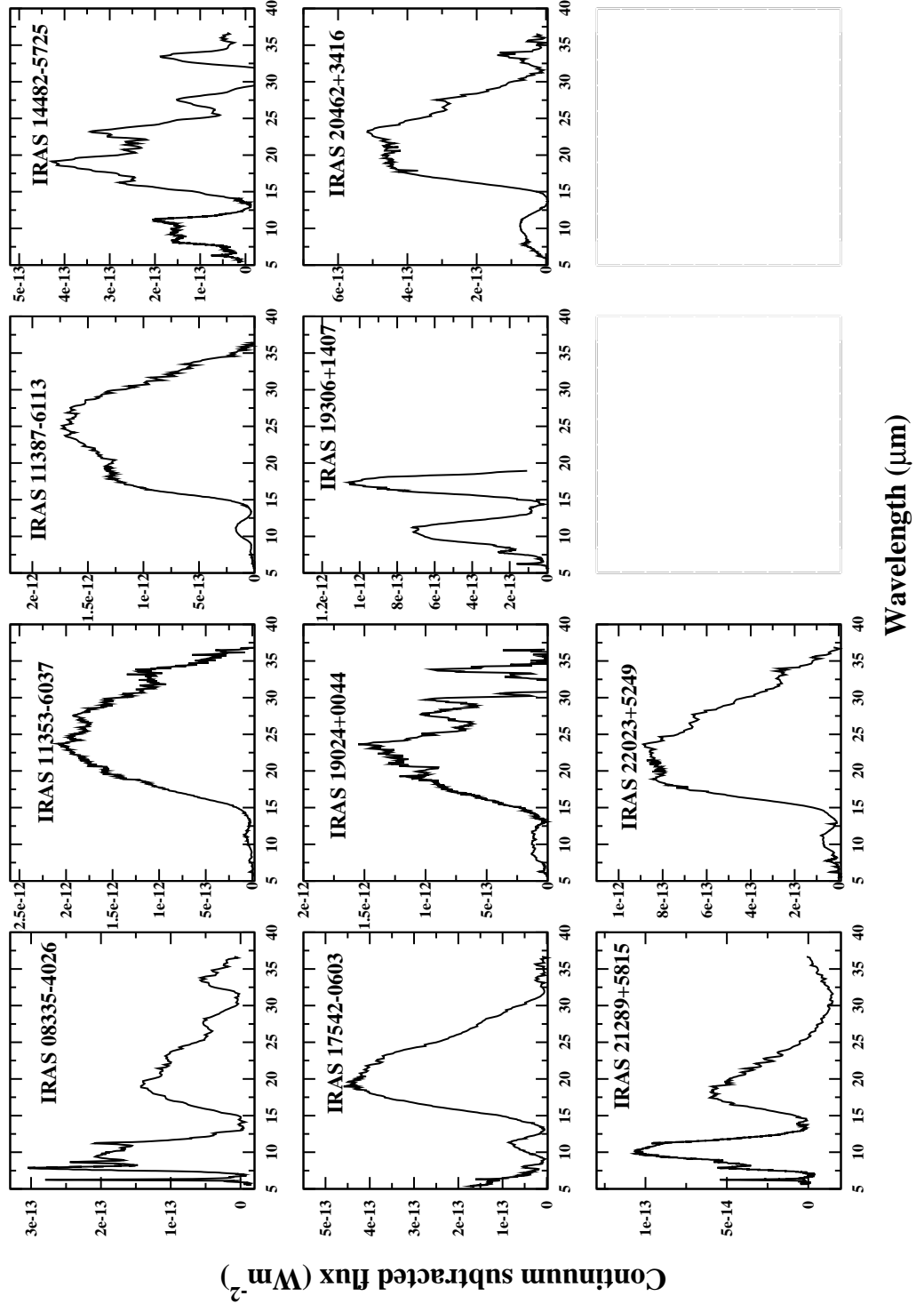


Figure A3. Continuum-subtracted *Spitzer* IRS spectra for sources with PAH and silicate emissions (Class 2b)

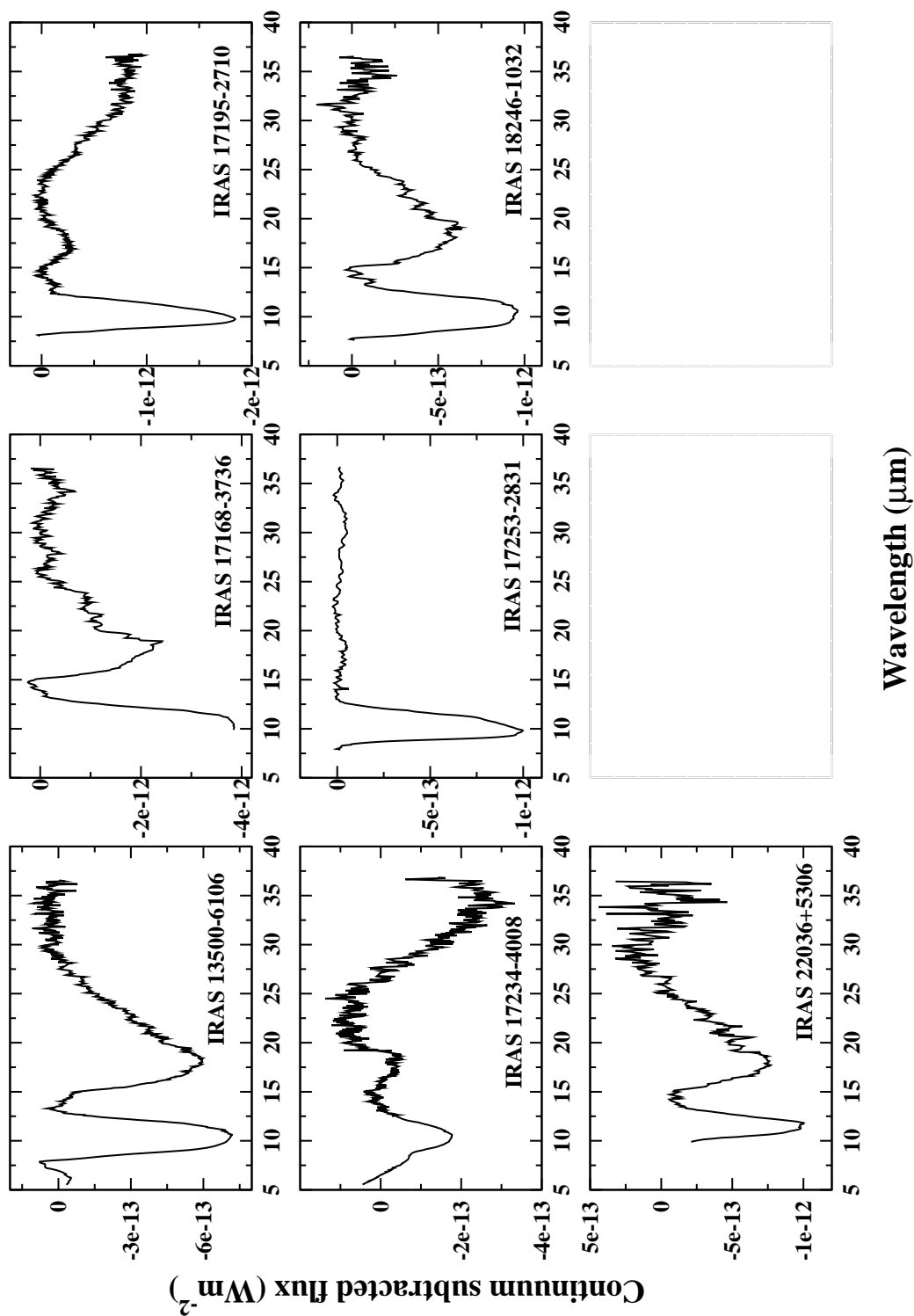


Figure A4. Continuum-subtracted *Spitzer* IRS spectra for sources with silicate absorption (Class 3)

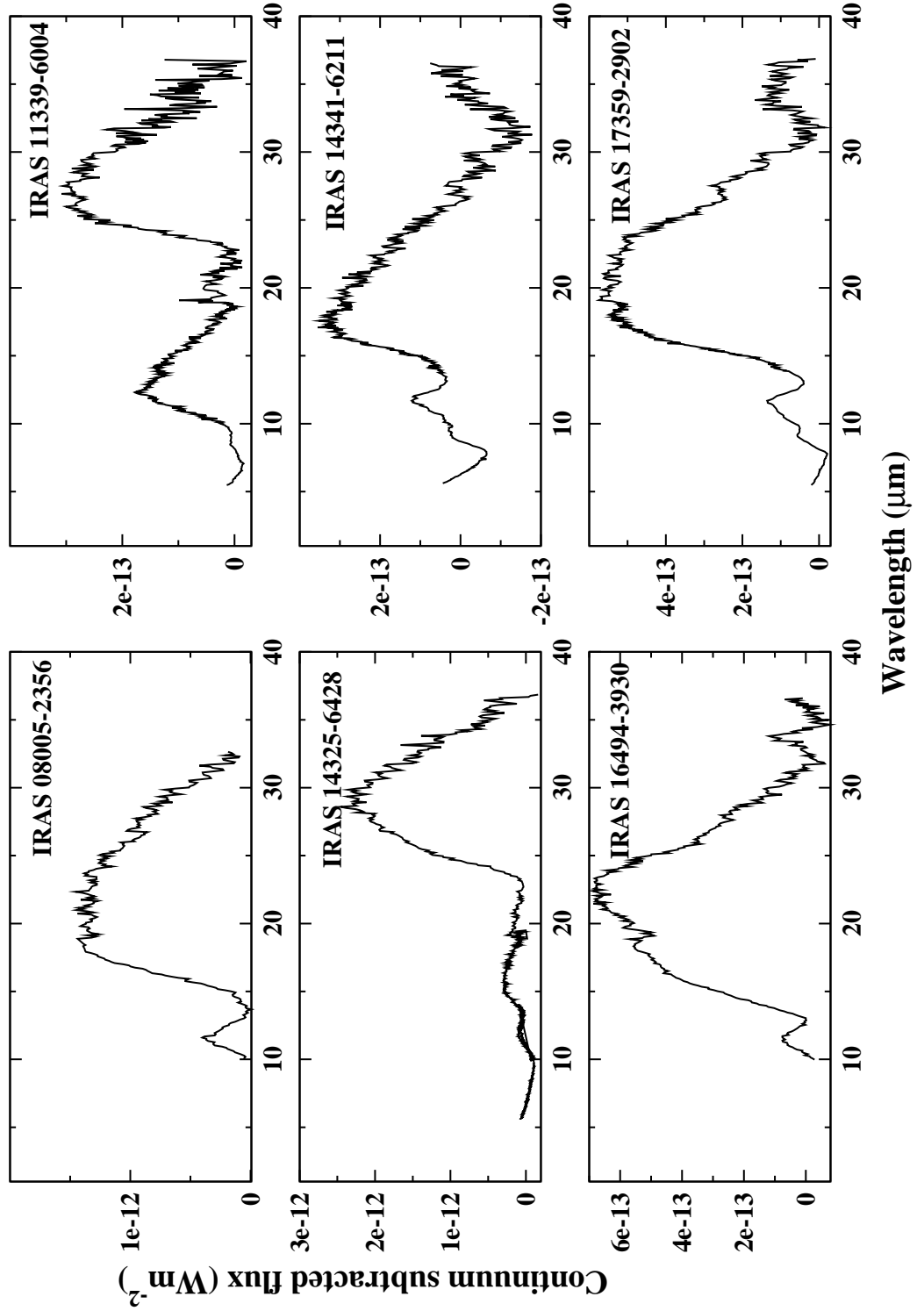


Figure A5. Continuum-subtracted *Spitzer* IRS spectra for sources with a broad $11\ \mu\text{m}$ emission (Class 4)

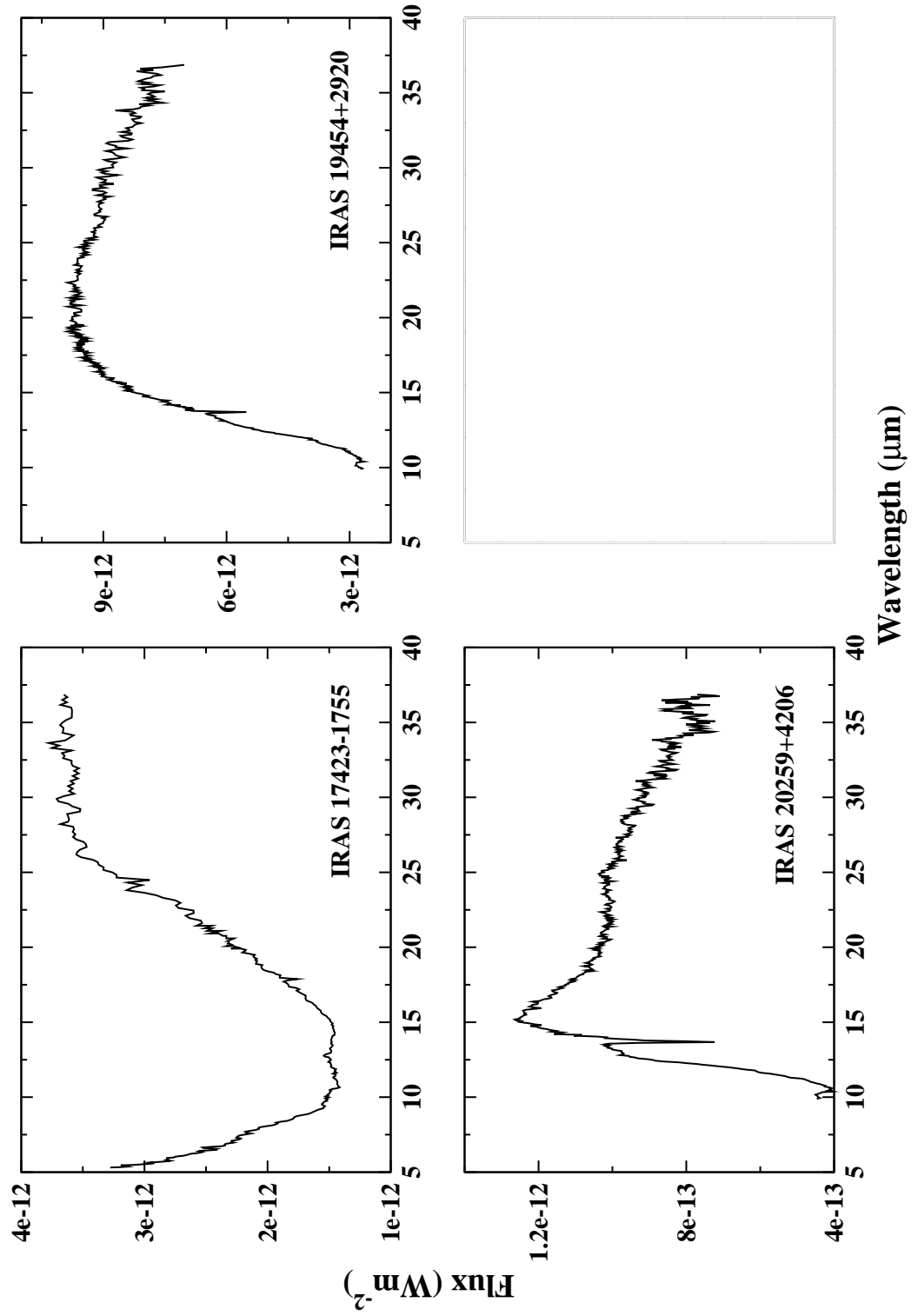


Figure A6. *Spitzer* IRS spectra for sources with featureless dust continuum (Class 5)

